UNIVERSITÉ CAEN NORMANDIE

Erasmus Mundus JMD on Nuclear Physics

Co-funded by the Erasmus+ Programme of the European Union

Enhancing Data Quality for the KM3NET-ORCA Detector.

Erasmus Mundus Joint Master degree in Nuclear Physics

Abhishek Sharma

Supervisors: Chiara Lastoria, Benoît Guillon

Date: September 6, 2024

Laboratoire de Physique Corpusculaire (LPC) - Caen
Université de Caen Normandie

Abstract

In this work, I discuss neutrino oscillations, focusing primarily on atmospheric neutrino oscillations within the context of the KM3NeT detector. I then address the unresolved issue of the Neutrino Mass Hierarchy (NMH), which refers to the unknown ordering of neutrino masses. The main objective of the KM3NeT detector is to determine the NMH by utilizing its deep-sea array of photomultipliers to detect atmospheric neutrinos. Additionally, I outline the two primary background sources specific to the KM3NeT detector.

I briefly discuss the simulation and experimental data, along with a summary of the reconstruction algorithms used. This report then explores the analysis of the reconstruction results produced by two algorithms, evaluated under different selection criteria. The performance analysis of these algorithms is conducted through simulations of both neutrinos and atmospheric muons, assessing their effectiveness in reconstructing key variables. Finally, the Data/MC ratio is examined across a sample of runs under different conditions to evaluate the consistency and accuracy of the simulations. Based on these findings, improvements could be applied to future simulations.

Contents

List of Figures

Chapter 1

Theoretical Introduction and KM3NET-ORCA

Neutrinos are elementary particles with no electric charge and half-integer spin, i.e. they are fermions. The (electron) neutrino was first postulated by Pauli in 1930 and its existence was proven by Reines and Cowan in 1956. Since then, two further neutrino flavours have been discovered, namely muon neutrino and tau neutrino. These particles are grouped within the Standard Model of elementary particle physics into three lepton generations, corresponding to the three quark generations. For each of these fermions, there exists an antiparticle partner. In the Standard Model, neutrinos are assumed to be massless. However, the observation of neutrino oscillations implies that neutrinos have non-zero masses.

1.1 Neutrino Oscillations

Neutrinos have the peculiar feature that the flavour eigenstates are different from the mass eigenstates. The three flavour eigenstates are a mixture of the three mass eigenstates with unequal masses. This leads to a phenomenon called neutrino oscillation, which refers to the periodic change of the probability of a neutrino produced in an eigenstate α to be detected in another eigenstate β.

1.1.1 Three Neutrino Mixing, the PMNS Matrix and the Neutrino Standard Model

The three flavour eigenstates, denoted as $|\nu_\alpha\rangle$ with $\alpha = e, \mu, \tau$ are the eigenstates of the weak interaction. Hence, neutrinos are always created as a pure flavour eigenstate and have to be projected onto these eigenstates whenever they interact.

The three mass eigenstates, denoted as $|\nu_k\rangle$ with k = 1, 2, 3, describe the free particle evolution and are the eigenstates of the corresponding Hamiltonian. These eigenstates have to be considered when describing the propagation of neutrinos in vacuum. In matter, the Hamiltonian and mass eigenstates are modified due to the matter potential(see Section 1.1.3). The mixing between the neutrino flavor eigenstates and the mass eigenstates is given by the following relation:

$$|\nu_\alpha\rangle = \sum_i U^*_{\alpha i} |\nu_i\rangle \tag{1.1}$$

$$|\nu_i\rangle = \sum_\alpha U_{\alpha i} |\nu_\alpha\rangle \tag{1.2}$$

where U is a 3×3 unitary matrix called Pontecorvo-Maki-Nakagawa-Sakata (PMNS), and can be parameterized by the mean of the three mixing angles, θ_{ij}, chosen to be confined as $0 \leq \theta_{ij} < \pi/2$, and a CP-violating phase, δ. [4] It can be decomposed into a product of three real rotation matrices, parametrized by mixing angles θ_{12}, θ_{13} and θ_{23}, and a diagonal matrix involving a complex phase $e^{i\delta_{CP}}$. The standard parametrization of the PMNS matrix is:

$$U = \begin{pmatrix} 1 & 0 & 0 \\ 0 & c_{23} & s_{23} \\ 0 & -s_{23} & c_{23} \end{pmatrix} \begin{pmatrix} 1 & 0 & 0 \\ 0 & 1 & 0 \\ 0 & 0 & e^{i\delta_{CP}} \end{pmatrix} \begin{pmatrix} c_{13} & 0 & s_{13} \\ 0 & 1 & 0 \\ -s_{13} & 0 & c_{13} \end{pmatrix} \begin{pmatrix} c_{12} & s_{12} & 0 \\ -s_{12} & c_{12} & 0 \\ 0 & 0 & 1 \end{pmatrix} \tag{1.3}$$

$$= \begin{pmatrix} c_{12}c_{13} & s_{12}c_{13} & s_{13}e^{-i\delta_{CP}} \\ -s_{12}c_{23} - c_{12}s_{13}s_{23}e^{i\delta_{CP}} & c_{12}c_{23} - s_{12}s_{13}s_{23}e^{i\delta_{CP}} & c_{13}s_{23} \\ s_{12}s_{23} - c_{12}s_{13}c_{23}e^{i\delta_{CP}} & -c_{12}s_{23} - s_{12}s_{13}c_{23}e^{i\delta_{CP}} & c_{13}c_{23} \end{pmatrix} \tag{1.4}$$

with the short notations:

$$c_{ij} \equiv \cos\theta_{ij},\ s_{ij} \equiv \sin\theta_{ij} \tag{1.5}$$

1.1.2 Three Flavor Oscillations in Vacuum

Neutrino oscillations are interpreted as an interference phenomenon since the three mass eigenstates have different masses (hence different energies), thus they propagate as waves with different frequencies. Accordingly, we can express the neutrino flavor eigenstate in terms of the time evolution operator as:

$$|\nu_\alpha(t)\rangle = \sum_i U^*_{\alpha i} |\nu_i(t)\rangle = \sum_i e^{-iE_i t} U^*_{\alpha i} |\nu_i\rangle = \sum_i e^{-iE_i t} U^*_{\alpha i} U_{\beta i} |\nu_\beta\rangle \tag{1.6}$$

Thus, the oscillation probability between the neutrino flavours α and β will be expressed as:

$$P_{\alpha\to\beta} = |\langle\nu_\beta|\nu_\alpha(t)\rangle|^2 = \sum_{i,j} e^{-i(E_i - E_j)t} U^*_{\alpha i} U_{\alpha j} U_{\beta i} U^*_{\beta j} \tag{1.7}$$

In the relativistic case, the eigen energies can be simplified as:

$$E_i = \sqrt{p^2 + m_i^2} \sim E + \frac{m_i^2}{2E} \tag{1.8}$$

where we have used the convention $c = \hbar = 1$, and since in an actual experiment what is measured is the distance traveled by the neutrino and not the time, one gets:

$$P_{\alpha\to\beta} = \sum_{i,j} U^*_{\alpha i} U_{\alpha j} U_{\beta i} U^*_{\beta j} e^{-i\frac{\Delta m^2_{ij}}{2E}L} \tag{1.9}$$

In the 3ν framework, the $\nu_\mu \leftrightarrow \nu_e$ and $\nu_\mu \leftrightarrow \nu_\tau$ transition probabilities in vacuum can be approximated by the following formulae:

$$P_{3\nu}(\nu_\mu \to \nu_e) \approx \sin^2\theta_{23} \sin^2 2\theta_{13} \sin^2\left(\frac{\Delta m^2_{31} L}{4E_\nu}\right) \tag{1.10}$$

$$P_{3\nu}(\nu_\mu \to \nu_\tau) \approx \cos^4\theta_{13} \sin^2 2\theta_{23} \sin^2\left(\frac{\Delta m^2_{31} L}{4E_\nu}\right) \tag{1.11}$$

And the formula for muon neutrino disappearance ($\nu_\mu \leftrightarrow \nu_\mu$) is given by:

$$P_{3\nu}(\nu_\mu \to \nu_\mu) \approx 1 - 4\cos^2\theta_{13} \sin^2\theta_{23}(1 - \cos^2\theta_{13}\sin^2\theta_{23}) \sin^2\left(\frac{\Delta m^2_{31} L}{4E_\nu}\right) [5] \tag{1.12}$$

1.1.3 Three Flavor Oscillations in Matter

Neutrinos propagating through normal matter can scatter off electrons and nucleons. These possible interactions give rise to an effective potential which neutrinos are experiencing. This effect is know as coherent forward scattering. The result is that neutrinos in matter have different effective masses than neutrinos in vacuum.

In the case of neutrino propagation in vacuum, the propagation Hamiltonian H is diagonal and given by:

$$H = \begin{pmatrix} E_1 & 0 & 0 \\ 0 & E_2 & 0 \\ 0 & 0 & E_3 \end{pmatrix} \tag{1.13}$$

However, when neutrinos travel through a medium, there is an additional term coming from the presence of electrons in the matter. This new term is diagonal in the flavor state basis [6]. Thus the Hamiltonian in matter in the electroweak basis is given by:

$$H_m = U \begin{pmatrix} 0 & 0 & 0 \\ 0 & \frac{\Delta m^2_{21}}{2E} & 0 \\ 0 & 0 & \frac{\Delta m^2_{31}}{2E} \end{pmatrix} U^\dagger + \begin{pmatrix} A(x) & 0 & 0 \\ 0 & 0 & 0 \\ 0 & 0 & 0 \end{pmatrix} \tag{1.14}$$

Where U is the neutrino mixing matrix in the vacuum. The mass squared differences are defined as $\Delta m^2_\odot \equiv m^2_2 - m^2_1 (\approx 7.5 \times 10^{-5} \text{eV}^2$ and $\Delta m^2_a \equiv m^2_3 - m^2_1 \approx \pm 2.5 \times 10^{-3} \text{eV}^2$, positive sign is for normal mass ordering and negative sign for inverted one). Here $A(x)$ is an effective potential $A = \pm \sqrt{2} G_F N_e$, where N_e is the electron number density of the medium, G_F is the Fermi constant and the $\pm$ sign is for ν_e and $\bar{\nu}_e$. [5, 6]

Once matter effects come into existence along the neutrino propagation path, and contrarily to the remaining flavors, the ν_e can experience interactions through the CC elastic scattering interactions with the electrons in matter and acquire the effective potential $V_{CC} = \pm \sqrt{2} G_F N_e$.

In the case of neutrinos propagating in a medium with constant density, the transition probabilities now read as follows [where the superscripts (m.e.) for the various parameters denote their values under the matter effect] [5]:

$$P^{m.e.}_{3\nu}(\nu_\mu \to \nu_e) \approx \sin^2\theta_{23} \sin^2 2\theta^{m.e.}_{13} \sin^2\left(\frac{\Delta^{m.e.} m^2 L}{4E_\nu}\right), \tag{1.15}$$

and:

$$P^{m.e.}_{3\nu}(\nu_\mu \to \nu_\mu) \approx 1 - \sin^2 2\theta_{23} \cos^2\theta^{m.e.}_{13} \sin^2\left(\frac{(\Delta m^2_{31} + \Delta^{m.e.} m^2)L}{8E_\nu} + \frac{AL}{4}\right) \tag{1.16}$$

$$- \sin^2 2\theta_{23} \sin^2\theta^{m.e.}_{13} \sin^2\left(\frac{(\Delta m^2_{31} - \Delta^{m.e.} m^2)L}{8E_\nu} + \frac{AL}{4}\right) \tag{1.17}$$

$$- \sin^4\theta_{23} \sin^2 2\theta^{m.e.}_{13} \sin^2\left(\frac{\Delta^{m.e.} m^2 L}{4E_\nu}\right) \tag{1.18}$$

Where, in the case of the matter, we have effective neutrino mixing parameter $\theta^{m.e.}$ given by:

$$\sin^2 2\theta^{m.e.}_{13} \equiv \sin^2 2\theta_{13} \left(\frac{\Delta m^2_{31}}{\Delta^{m.e.} m^2}\right)^2, \tag{1.19}$$

$$\Delta^{m.e.} m^2 \equiv \sqrt{(\Delta m^2_{31} \cos 2\theta_{13} - 2E_\nu A)^2 + (\Delta m^2_{31} \sin 2\theta_{13})^2} \tag{1.20}$$

where A is positive for neutrinos and negative for antineutrinos. Both the amplitude and the phase of the oscillations can therefore be affected by matter effects.

1.1.3.1 Resonance enhancement and MSW effect

In certain conditions the oscillations can become resonant, meaning that the effective mixing is maximal, i.e $\Delta^{m.e.}m^2$ is minimal. These conditions correspond to a match of the neutrino energy E and electron density in matter N_e. In addition, the resonance occurs selectively either for neutrinos or for antineutrinos depending on the mass ordering. Indeed, with our convention, if$\Delta m^2 > 0$, the oscillation amplitude becomes maximum only for neutrinos, and if $\Delta m^2 < 0$, only for antineutrinos. The sign of Δm^2, which had no effect in vacuum, becomes observable with matter effects (For more details see [5].

1.1.4 Measuring Neutrino Mass Hierarchy

Although the absolute values of the mass-squared differences between different mass eigenstates are known from oscillation experiments, it is still unknown how the neutrino masses eigenstates are arranged relative to each other on the mass scale, i.e. the signs of the mass-squared differences. This is called neutrino mass hierarchy (NMH).

The convention is to choose m_1 and m_2 as the mass eigenstate that are close to each other, with $m_1 < m_2$. The third mass eigenstate is separated from the other two, either above or below. The ordering $m_1 < m_2 < m_3$ is customary referred to as normal hierarchy (NH) and $m_3 < m_1 < m_2$ as inverted hierarchy (IH). Both possible neutrino mass hierarchies (NMH) scenarios are illustrated in Figure 1.1. Additionally, the flavour composition of the three mass eigenstates are shown.

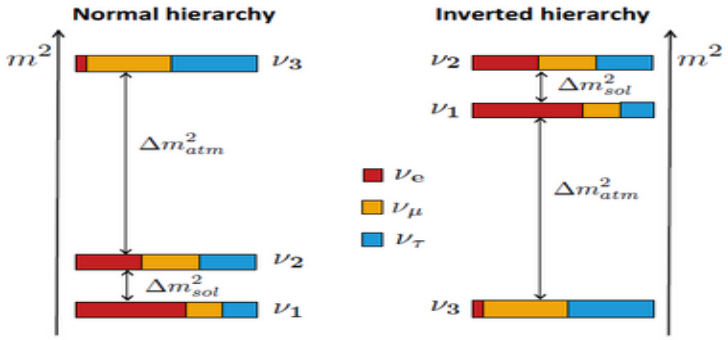

Figure 1.1: The normal and inverted scenarios for the neutrino mass hierarchy. The color code indicates the fraction of each flavor (e, μ, τ) present in each of the mass eigenstates (1, 2, 3). Note that the spacing between mass eigenstates on the vertical axis does not scale exactly with the measured Δm^2 values.

In the first plot below in Fig. 1.2, we see the oscillogram for electron neutrinos, with the cosine of zenith angle (see Figure 1.6) on the vertical axes. The horizontal demarcations denote the boundaries between the different Earth layers [7], and thus it can be noted that in the Normal Hierarchy, we observe the effect of electron resonance for neutrinos, and for the Inverted Hierarchy, the effect is observed on the anti-neutrinos.

A promising pathway to NMH measurement are atmospheric neutrino experiments probing neutrino oscillation in the Earth. This experimental approach is pursued by the KM3NeT collaboration, which plans to build a megaton-scale underwater Cherenkov detector named ORCA in the Mediterranean Sea. Measuring the NMH from the oscillations of atmospheric neutrinos requires to probe the MSW-resonant energy range. The NMH affects both the amplitude and phase of the oscillations, with the strongest impact in the resonance region $E_\nu \sim$ (4–8) GeV.

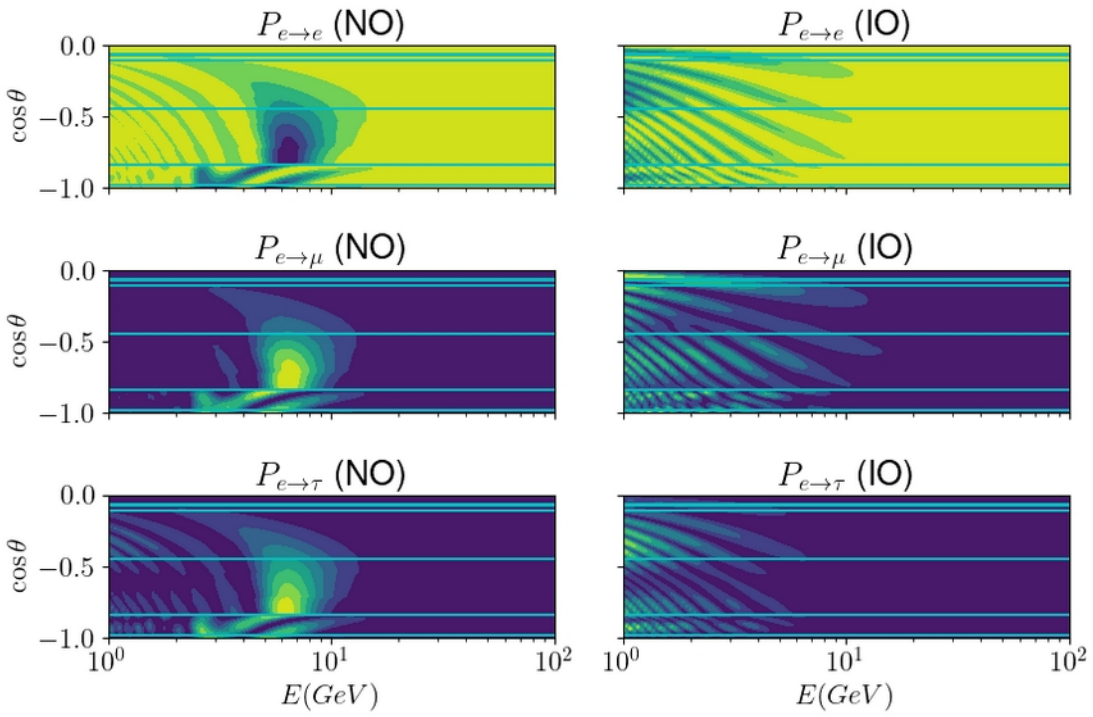

Figure 1.2: Oscillogram for electron neutrinos in Normal Ordering(left) and Inverted Ordering(right), with cosine of direction angles on the vertical axes, and the horizontal demarcations denoting the Earth layer boundaries.

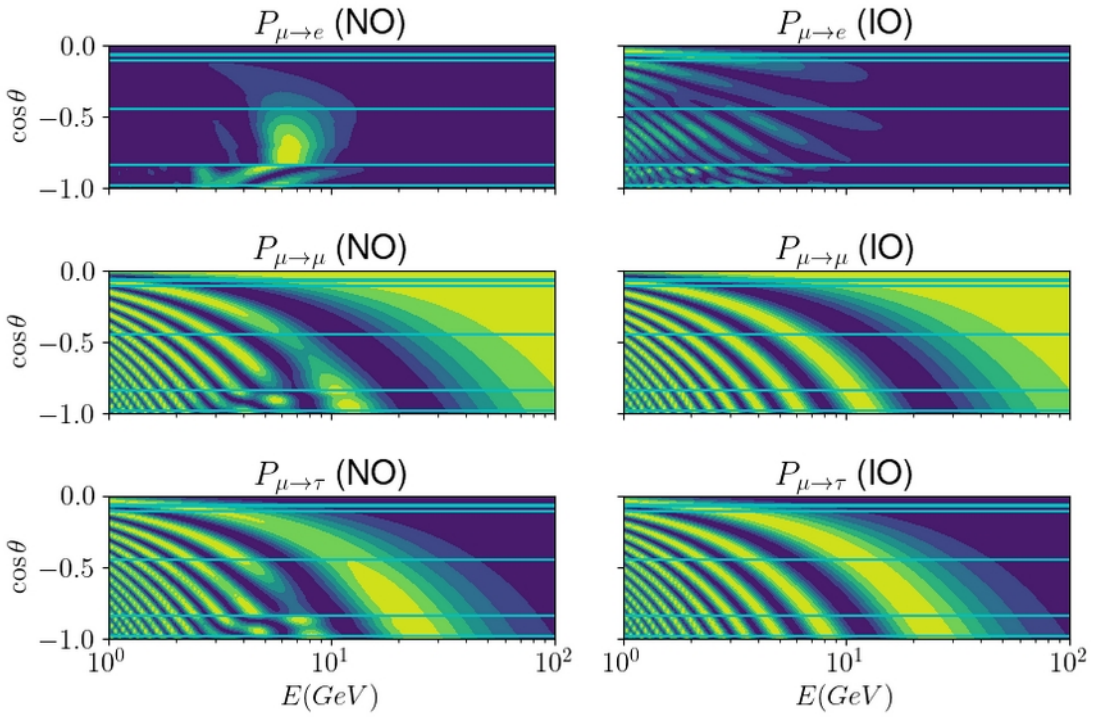

Figure 1.3: Oscillogram for muon neutrinos in Normal Ordering (left) and Inverted Ordering (right), with the cosine of the direction angles on the vertical axes. The horizontal demarcations denote the boundaries between the different Earth layers.

1.2 Atmospheric neutrinos

Atmospheric neutrinos are created by the interaction of cosmic rays (CR) (mostly protons and light nuclei such as helium) with nuclei in the upper part of the atmosphere. In a manner similar to the production of an artificial neutrino beam at a particle accelerator, the incoming cosmic rays (referred to as the primary CR) are highly energetic (up to 10^{20} eV), while in comparison the target nuclei in gas molecules are essentially at rest. The collisions produce the so-called secondary CR, which includes a variety of hadrons – in particular, pions and kaons. Below 100 GeV, the main contribution comes from $\pi^{\pm}$ decays, but the contribution of $K^{\pm}$ decays increases progressively with energy. For the most part, neutrino production occurs in the lower stratosphere ($\sim$ 10-30 km).

The electron-to-muon flavour ratio is about 1:2, due to the dominant chain of production processes formed by the charged meson decay:

$$\pi^+/K^+ \longrightarrow \mu^+ + \nu_\mu \tag{1.21}$$

$$\pi^-/K^- \longrightarrow \mu^- + \bar{\nu}_\mu \tag{1.22}$$

Depending on the energy, muons are the main component of the flux of charged secondary CR seen at the Earth's surface. They are referred to as atmospheric muons or sometimes as cosmic muons (though the muon component in the primary cosmic ray flux is very small). Nevertheless, a significant number of them decay before reaching us, producing two neutrinos per decay:

$$\mu^+ \longrightarrow e^+ + \nu_e + \bar{\nu}_\mu \tag{1.23}$$

$$\mu^- \longrightarrow e^- + \bar{\nu}_e + \nu_\mu \tag{1.24}$$

The flux of atmospheric neutrinos, therefore, contains ν_e, $\bar{\nu}_e$, ν_μ and $\bar{\nu}_\mu$ (τ leptons are not produced in significant quantities in the secondary CR because of the tau lepton being heavier than $\pi/K^{\pm}$, thus the $\nu_\tau/\bar{\nu}_\tau$ component is negligible). Their energy ranges from $\sim$0.1 GeV up to very high energies (since the maximal energy of the primary CR is extremely high), with a steeply decreasing energy spectrum.

Thus, the atmospheric neutrino production can be summarised by the equations below:

$$\pi^+/K^+ \Longrightarrow \nu_\mu + \bar{\nu}_\mu + \nu_e \tag{1.25}$$

$$\pi^-/K^- \Longrightarrow \bar{\nu}_\mu + \nu_\mu + \bar{\nu}_e \tag{1.26}$$

As a consequence of the overabundance of matter over antimatter in the cosmic ray primaries and secondaries, the $\nu_e/\bar{\nu}_e$ ratio is roughly equal to 1.3, with a moderate dependence on both energy and zenith angle. On the contrary, the $\nu_\mu/\bar{\nu}_\mu$ ratio shows a clear increase with energy and a zenith angle dependence. This is again related to the decrease of the contribution of muon decays, which are responsible for washing out the μ^-/μ^+ asymmetry.

Another effect comes into play at higher energies. While (1.21) and (1.22) is an almost exclusive decay channel for $\pi^{\pm}$ (99.9%), the branching ratio (BR) of this channel for charged kaons $K^{\pm}$ is only 63.6%. The other decays producing neutrinos are semileptonic:

$$K^+ \longrightarrow \pi^0 + \mu^+ + \nu_\mu \qquad (3.4\%) \tag{1.27}$$

$$K^+ \longrightarrow \pi^0 + e^+ + \nu_e \qquad (5.1\%) \tag{1.28}$$

In the case of (1.28), the chain ends, only producing one ν_e overall. The flavor ratio thus depends on the ratio of $\pi^{\pm}$ to $K^{\pm}$ production in the hadronic processes(see [8] for more details).

1.3 The KM3NeT/ORCA detector

KM3NeT represents a novel Research Infrastructure hosting a network of deep-sea neutrino telescopes situated in the Mediterranean Sea. This infrastructure serves a dual purpose: initially, it aims to discover and subsequently observe high-energy neutrino sources in the Universe. Additionally, it seeks to determine the mass hierarchy of neutrinos. The fulfillment of the first objective relies on the ARCA facility (Astroparticle Research with Cosmics in the Abyss), while the second objective is addressed by ORCA (Oscillation Research with Cosmics in the Abyss). The deep-sea locations—off-shore Toulon (France) and Capo Passero (Sicily, Italy) — have been strategically chosen based on the optical properties of the water, distance to shore, and local infrastructure. [5]

1.3.1 Digital optical module

The 'digital optical module' (DOM) developed by the KM3NeT collaboration comprises a transparent 17-inch diameter pressure-resistant glass sphere, housing 31 3-inch PMTs, their associated readout electronics and additional sensors. Pictures of the DOM and PMT are shown in Fig. 1.4. The PMTs are strategically positioned in a 3D printed support structure, arranged in 5 rings of 6 equally spaced PMTs and a single PMT pointing vertically downward in the upper hemisphere, totaling 12 PMTs, and 19 PMTs in the lower hemisphere. A reflector ring around each PMT's face enhances photon collection efficiency, and optical gel ensures optical contact between the PMT photocathode, reflector ring, and glass sphere.

A distinctive feature of the KM3NeT optical module is the multi-PMT design, setting it apart from traditional designs using single larger PMTs, as seen in ANTARES or IceCube. The segmentation of the photocathode area in the multi-PMT design provides advantages, including directional information for photon arrival direction, improved event reconstruction, high efficiency in detecting multiple photons, and enhanced optical background rejection capabilities—all achieved at a reduced cost per unit of photocathode area.

Figure 1.4: Photographs of a KM3NeT DOM (left) and Hamamatsu R12199-02 photomultiplier tube (right). In the DOM, the visible part of the individual PMTs comprises the photocathode areas, circled by the silver-colored reflector rings.

1.3.2 Detection Unit and detector layout

Detection Units (DUs) in the KM3NeT are composed of 18 Digital Optical Modules (DOMs) arranged along vertical, flexible string structures. Each DU is upheld by two parallel fiber ropes connected to a

seafloor anchor, ensuring vertical alignment even in strong sea currents. An electro-optical cable running vertically along the strings supplies power and facilitates optical data transmission from the DOMs to the seabed infrastructure.

In ARCA and ORCA, the vertical and horizontal spacing between DOMs varies due to differences in targeted neutrino energy. ORCA's vertical spacing, optimized for the NMH physics study [5], slightly varies between successive storeys (8.7, 9.4, 10.9 m) to accommodate the furling of the string during deployment. The horizontal spacing adheres to a minimum requirement of 20m, with neighboring strings distributed around an average of 23m, ensuring safe deployment and detector operation.

Fig. 1.5 displays the latest ORCA detector layout, illustrating the electro-optical cables (MEOC) that gather optical fibers and power supply, transmitting data from shore to the detector site.

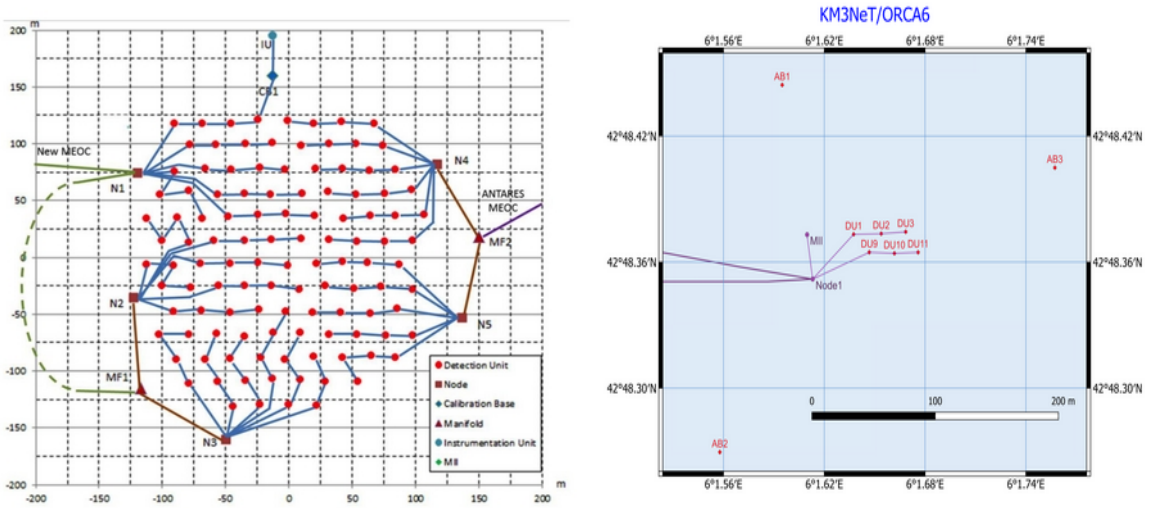

Figure 1.5: **Left:** Footprint of the planned layout of the ORCA detector (top view). The 115 DUs are represented as red dots and the power supply and optical-fibre connections between the DU bases as blue lines. Each chain of 4 DUs is connected to a node, where the optical signal is multiplexed. Each node controls in total 24 DUs and is connected either to the next node or to one of the two main electro-optical cables (MEOC). **Right:** Layout of the ORCA6 detector configuration. The dots labelled as DU n in the diagram represent detection units, connected to the node.

Figure 1.6 represents the convention used for zenith angle. The cosine $\cos\theta$ is often used instead of θ_z (sometimes simply θ).

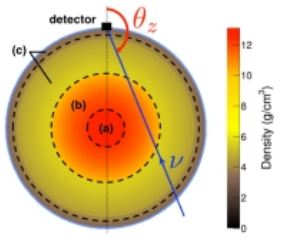

Figure 1.6: Zenith Angle

Direction	θ_z	$\cos\theta$
vertical upgoing	π (180)	-1
horizontal upgoing	$\frac{\pi}{2}$ (90°)	0
vertical downgoing	0 (0°)	1

1.3.3 Background

There are several different types of background sources obscuring the neutrino signature in Cherenkov detectors. Two classes can be differentiated: optical noise and atmospheric muons.

1.3.3.1 Optical noise

This noise originates from three sources:

- **^{40}K decays:** Seawater contains a small amount ($\sim$0.04%) of the radioactive isotope Potassium-40 (^{40}K), which can decay to ^{40}Ca via β-decay (branching ratio 89.3%) or to ^{40}Ar via electron capture (branching ratio 10.7%). The resulting electron from the β-decay has a maximal energy of 1.33 MeV, which is sufficient to emit Cherenkov light. The photon emitted by the excited ^{40}Ar state has an energy of 1.46 MeV, which can be converted into Compton electrons capable of emitting Cerenkov light.

- **Dark count rate :** The dark count rate is the counting rate by the photosensors measured in the absence of external light sources. It includes the thermally-generated noise of the PMT and usually also the radioactive decays in the glass and the optical gel (mainly ^{40}K decay).

- **Bioluminescence :** The deep sea is inhabited by a large diversity of luminescent organisms, which emit visible light as a result of a chemical reaction [3]. For deep-sea Cherenkov detectors, this light shows a slowly-changing background rate in the entire detector. On top of the baseline rate, light bursts with duration of up to several seconds are observed on neighbouring photo-sensors. Bright bioluminescence bursts can exceed the ubiquitous background rate up to several tens of metres away from the light-emitting organisms. Bioluminescence activity shows noticeable seasonal variations.

1.3.3.2 Atmospheric muons

In the development of cosmic-ray air showers, muons are produced besides neutrinos. These muons are called atmospheric muons. Most of them are stopped in the overburden above the detector, however, with sufficient energy ($\geq$ 500 GeV for 2 km water equivalent), muons can reach the detector from above.

The signature of few-GeV muons in water Cherenkov detectors is a straight track with a nearly uniform luminance. The length of the track is approximately 4m/GeV in water. As muons cannot transverse the Earth, no atmospheric muon can reach the detector from below. Thus, all upgoing events have to be induced by neutrinos interacting in the detector or its vicinity. Nevertheless, misreconstructed atmospheric muons can mimic an upgoing event signature and may fake a neutrino-induced signal event. Therefore, a good accuracy in the event selection is needed in order to reduce this background[2].

Chapter 2

Simulation, Data Analysis and Results

The primary objective of the study is to assess the quality of the collected data and ensure its stability over time (i.e. studying the background). This is achieved through data and Monte Carlo (MC) comparisons. If a particular run exhibits poor agreement between the data and the MC simulations, it is discarded to maintain the integrity of the analysis. For each event recorded in the experiment, several key variables are reconstructed using two distinct algorithms (as detailed in Section 2.2). In addition to these reconstructed variables, additional information is stored, such as the number of triggered Photomultiplier Tubes (PMTs) for each event.

The variables reconstructed for each event include the energy E (which could correspond to an atmospheric muon, neutrino, or noise event), the direction (specified by the zenith and azimuth angles), and the position (in the case of neutrino events, this refers to the interaction vertex). Additionally, the likelihood is also calculated, providing a measure of the confidence in the reconstruction. To confirm the neutrino mass hierarchy, precise reconstruction of energy E and the cosine of the zenith angle($\cos\theta$) is crucial, as these variables directly affect neutrino oscillation patterns observed in the oscillograms (Figure 1.2 and 1.3). Along with E and $\cos\theta$ other complementary variables such as position and likelihood are also reconstructed.

In the first step, the simulation was analyzed, verifying the reconstruction of each variable mentioned above. The simulation and experimental data both are studied for different conditions mentioned in Table 2.1 in order to analyse the behaviour of each variable. For the performance comparison between two algorithms, the reconstruction for each variable is compared. At last, in order to study the Data/MC ratio for E and $\cos\theta$ the analysis is done run by run like mentioned in Section 2.1. The Data/MC ratio is studied under different selections to see how it changes, specially effect of condition "no of triggered PMTs more than 12".

2.1 Simulation and Experimental data collection

This section describes the simulation tools and the generation of simulated Monte Carlo (MC) events used for the results presented in this thesis. As you can see in Figure 1.5, there are 115 DUs planned for fully operational detector but the presented work is based on only 6 DUs (see Figure 1.5) not full detector. The simulation is conducted on a run-by-run basis due to the wide variability in background conditions across different runs (e.g. the seasonally-dependent presence of bioluminescent microorganisms). This approach allows for dynamic updates for initial conditions to the simulation parameters. By tailoring the Monte Carlo (MC) simulation to the unique background of each run, the accuracy and reliability of the simulated data are significantly improved, leading to more precise comparisons with the actual experimental data.

In the simulation chain a volume surrounding the instrumented volume, called "can", is defined. The can volume is a cylinder with height and radius exceeding the instrumented volume by about 3 absorption lengths for the atmospheric muon background simulation and by 40 m for the neutrino generation.

Generated particles are propagated inside the can and Cherenkov light is generated. For the simulation, there are 3 components : Neutrinos, two background sources : atmospheric muons and pure noise.

Neutrino induced interactions in sea water are simulated with gSeaGen, a software package based on the widely used GENIE (version 2.12.10) code. Neutrinos and antineutrinos in the energy range from 1 GeV to 100 GeV are simulated and weighted to reproduce the conventional atmospheric neutrino flux following the Honda model. All particles emerging from neutrino interactions are propagated with the GEANT4-based software package KM3Sim. Using this software, Cherenkov photons are generated from primary and secondary particles, tracked through the sea water taking into account absorption and scattering, and detected by the PMTs. The simulation for neutrinos contains all kinds of flavors.

Atmospheric muon events are generated using the MUPAGE package. The KM3 package is then used for tracking the muons in sea water and the subsequent Cherenkov light production. The PMT response and the readout are simulated using custom KM3NeT software. In this step, the optical background due to Cherenkov light from β-decays of ^{40}K in the sea water is also added [1].

The data-taking period for ORCA6 spans from January 2020 to November 2021. The data is taken continuously and divided into runs with a typical duration of 6 hours. There are total 3896 runs for that time duration. Data quality criteria were applied to exclude runs taken in unstable data-acquisition conditions. Due to stringent conditions applied to remove bioluminescence from the data, only 1804 out of 3896 recorded runs were retained. So this data sample corresponds to a very stable one in terms of low bioluminescence activity.

2.2 Reconstruction Algorithms

Neutral current (NC) neutrino interactions produce a neutrino and a hadronic shower, while charged current (CC) neutrino interactions result in a hadronic shower and a charged lepton. The events in KM3NeT/ORCA are classified into two categories: "track-like" events encompassing ν_μ CC events, ν_τ CC events followed by the tau lepton decaying into a muon (branching ratio of about 17%) and atmospheric muons; and "shower-like" events, comprising ν_e CC events, other decay channels of the tau lepton from ν_τ CC events, all flavour ν NC events and pure noise. The same classification scheme applies to antineutrinos. There are two reconstruction algorithms named jppmuon and jppshower optimized for the two main topologies of events (track and shower). This distinction is motivated by the different event topologies in the detector. As the name suggests jppmuon is optimized for track-like events (e.g. atmospheric muons) and jppshower algorithm is for shower-like events (e.g. background noise). Both algorithms are maximum likelihood fits and reconstruct the energy and direction as well as interaction vertex position and the time at which the light arrives on each PMT.

The algorithm follows specific steps during event reconstruction: it first determines the position of the vertex, then reconstructs the direction, and finally estimates the energy. If the algorithm successfully completes all these steps without failure, the event is classified as "reconstructed well". The jppmuon algorithm is applied to all events. However, the jppshower algorithm, which is computationally demanding, is only applied to a subset of events, those that are well-reconstructed and upgoing given by the jppmuon algorithm. This selective approach optimizes total amount of data to process as well. This strategy is particularly important because the signal of interest is overshadowed by downgoing cosmic muons, which dominate the data.

The digitised PMT output signal is typically called a hit. The information available for event reconstruction are a set of hits associated with the event. Each hit consists of the following pieces of information: position and orientation of the PMT that record the hit, a timestamp and a pulse charge information. The goal of event reconstruction is to determine the event hypothesis (being tracklike or showerlike) that most accurately matches the observed hit pattern [2].

2.3 General Analysis

The data analysis is done for different conditions mentioned in Table 2.1. First, here I will address the data analysis done with different conditions as follows :

	jppmuon	jppshower
condition	cut	
reconstructed well	cut 1	cut 3
reconstructed well + no of triggered PMTs more than 12	cut 2	cut 4
reconstructed well + no of triggered PMTs more than 12 + $\cos\theta_z$ given by both algorithm is less than zero	cut 5	

Table 2.1: Conditions for which data analysis is done

Cut 1 includes all well-reconstructed events by the jppmuon algorithm, while Cut 3 applies to well-reconstructed events by the jppshower algorithm, with additional optimization as described in Section 2.2. Cut 2 builds on Cut 1 by adding the condition "no of triggered PMTs more than 12", and similarly, Cut 4 extends Cut 3 with the same PMT condition. The intention behind this "no of triggered PMTs more than 12" condition is to reduce background noise while minimally impacting the neutrino flux.

Finally, Cut 5 is obtained by adding the requirement that the cosine of the zenith angle $\cos\theta_z$ reconstructed by both algorithms must be less than zero to Cut 4. This selection effectively removes events reconstructed as downgoing by both algorithms, targeting the elimination of downgoing atmospheric muons. However, it is possible that atmospheric muons can still be misreconstructed as upgoing by either algorithm.

2.4 Performance comparison

As mentioned before, there are 1804 runs which are analysed for all cuts. But the analysis for only cut 5 is mentioned here. Using cut 1, 2, 3, 4, we verified the reconstruction of each variable aforementioned (see Appendix A for more details). We also confirmed the impact of the "no of triggered PMTs more than 12" condition, as shown in Table 2.2. The table reveals that this condition significantly reduces pure noise, eliminating nearly 98% of events for both algorithms. For neutrinos, approximately 20% of events are removed by both algorithms, indicating a minimal effect on the neutrino flux. However, for atmospheric muons, the condition removes about 32% of events reconstructed by the jppshower algorithm and around 13% for the jppmuon algorithm. Thus, we effectively reduce background noise without significantly affecting the neutrino signal. For data, around 28% events for jppmuon and 82% events for jppshower are removed.

	jppmuon		jppshower	
	cut 1	cut 2	cut 3	cut 4
Neutrino	4099034	3288251 (80.22%)	2278579	1842605 (80.87%)
Muon ($\times 10^8$)	2.847315	2.472242 (86.82%)	0.1189198	0.080312 (67.53%)
Pure Noise	3674733	715 (0.01946%)	1863462	398 (0.02136%)
Data($\times 10^8$)	3.125041	2.266839 (72.54%)	0.3676283	0.06709757(18.25%)

Table 2.2: The effect of condition "no of triggered PMTs more than 12"

To evaluate the performance of both algorithms, the 1D distributions of the variables—energy (E), direction (zenith and azimuth angles), and vertex position (X, Y, Z)—reconstructed by both algorithms are compared under Cut 5. This comparison is done using simulations of atmospheric muons and neutrinos. We know that atmospheric muons are tracklike events so we expect jppmuon to perform better

whereas neutrinos have both topologies mixed. We also analyze 2D distributions of variables plotted true value of the variable against reconstructed one.

2.4.1 For Neutrinos

In this section, the results are reported for cut 5. All the 1D distributions (like Figure 2.1) are normalized. Figure 2.1 shows the reconstructed energy given by each algorithms. The distribution of reconstructed energy given by jppmuon is maximum around 9 GeV with a extra peak at higher energies. The reason for this peak is still under investigation. But for jppshower, it is centered around 20 GeV.

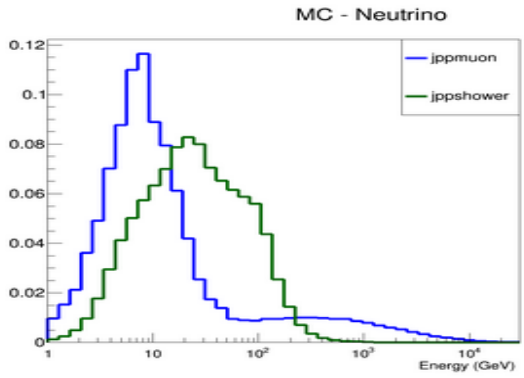

Figure 2.1: Energy(GeV) reconstruction

The 2D plot in Figure 2.2 displays the relationship between true neutrino energy and the reconstructed energy produced by the algorithm. In this figure, for each true energy value (represented as a bin on the x-axis), a distribution of reconstructed energy corresponding to that bin is provided by the algorithm. The right plot in Figure 2.2 illustrates the projection of bin number 38 from 2D plot on left. Notably, two peaks are visible, which is a characteristic of the jppmuon algorithm. The underlying cause of this behavior is still being investigated. Each projection is fitted with gaussian excluding the right peak for jppmuon algorithm as shown in the right plot of Figure 2.2. The mean and the standard deviation from the fit are 15.35 GeV, 4.16 GeV, respectively. These quantities are shown at the bin no 38 on x axis in the 2d plot (reco vs true). The same way for all the projections, mean and the standard deviation from the fit are shown in 2D plot. The ideal reconstruction is represented by the red diagonal line. The 2D plot indicates that linearity in the reconstructed energy is maintained up to 10 GeV; beyond this point, the reconstructed energy begins to deviate from perfect reconstruction. Above 100 GeV, saturation effects are observed.

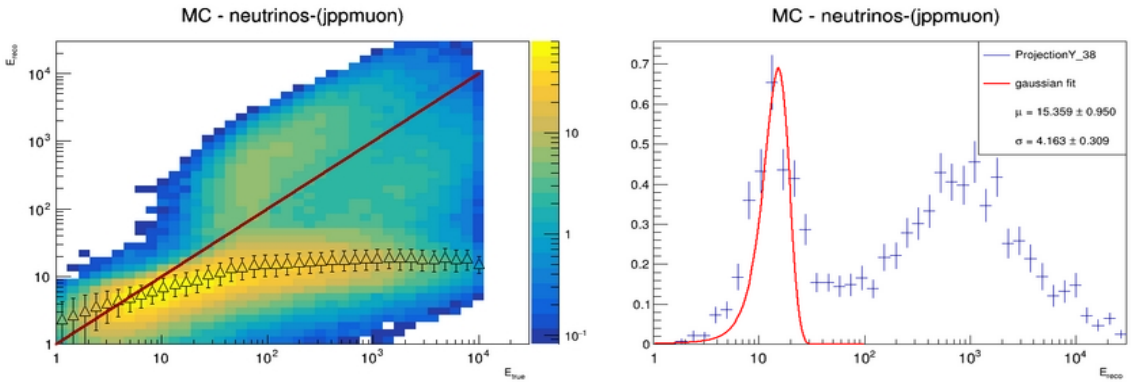

Figure 2.2: Energy (GeV) reconstruction (true vs reco)(left), The red line diagonally represents perfect reconstruction, Gaussian fit for the projection of bin no 38 (right) for jppmuon algorithm. The projection for jppmuon shows extra peak on right side which is still under investigation

The same procedure is followed for the energy reconstruction given by jppshower algorithm. The 2D plot (reco vs true) and projection of bin no 38 for jppshower are shown in Figure 2.3. The mean and the standard deviation from the fit are 108.59 GeV, 31.55 GeV, respectively. The 2D plot shows that for the jppshower algorithm, deviations occur at energies below 5 GeV and above 100 GeV, while linearity is maintained between this range.

By comparing the 2D plots of reconstructed versus true energy for both jppmuon and jppshower, we can conclude that the jppshower algorithm provides better energy reconstruction than the jppmuon algorithm.

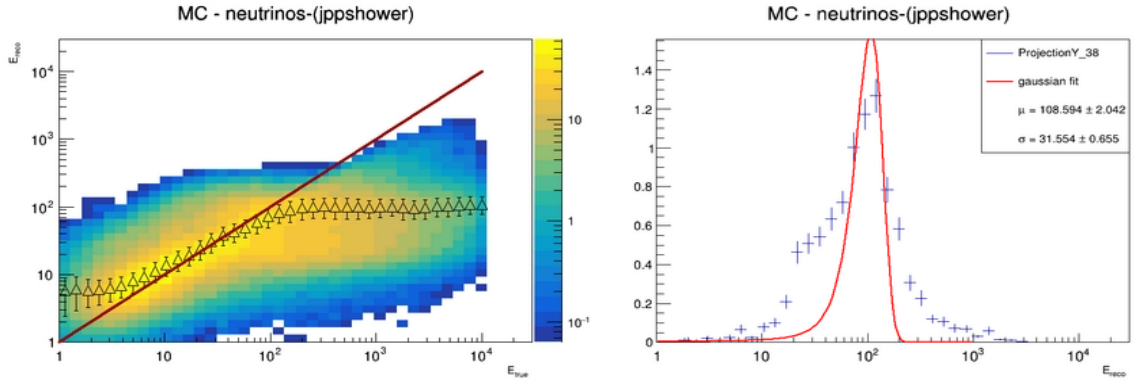

Figure 2.3: Energy(GeV) reconstruction (true vs reco)(left), The red line diagonally represents perfect reconstruction, Gaussian fit for the projection of bin no 38 (right) for jppshower algorithm respectively.

To get the performance quality, the variable ξ is plotted for cosine and position.

$$\xi = \frac{(reco - true)}{true} \tag{2.1}$$

where reco is the reconstructed value given by the algorithm for any true value of the variable. From now on, I will address this ratio as ξ. For the perfect reconstruction, this variable should be zero. For the good reconstruction, it should be centered around zero with a gaussian shape. It is fitted with the Gaussian function to get the bias and the spread of the distribution (as shown in right plot in Figure 2.4).

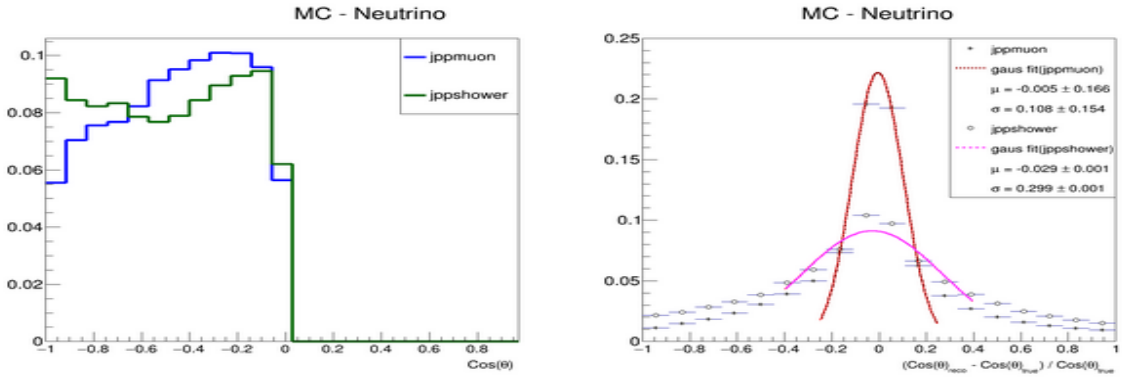

Figure 2.4: $\cos\theta$ reconstruction(left) and plot for ξ variable(right) for both algorithms.

Figure 2.4 presents the 1D distribution of reconstructed $\cos\theta$ for each algorithm. The plot on the left side of Figure 2.4 and the true versus reco plots in Figure 2.5 illustrate the selection criteria for cut 5. As outlined in Table 2.1, only events that are reconstructed as upgoing ($\cos\theta$)<0) by both algorithms are selected. From Figure 2.4, we get that the bias for jppmuon (-0.005) and for jppshower (-0.029) are not much different. so we can conclude that there is no inherent bias in the reconstruction provided by either algorithm. However, the ξ distribution for the jppshower algorithm exhibits a significantly larger

spread, with a value of 0.3, compared to the jppmuon algorithm's spread of 0.108. This indicates that the jppshower algorithm has more variability in its reconstruction.

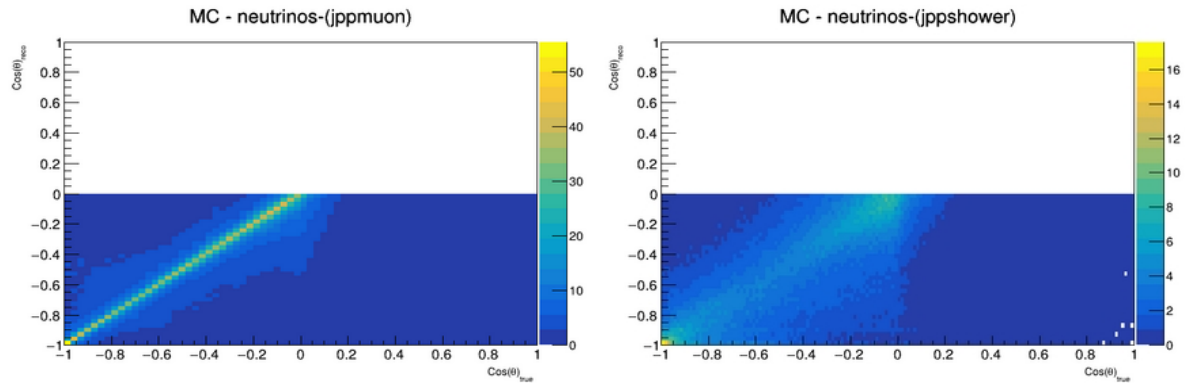

Figure 2.5: $\cos\theta$ reconstruction(true vs reco)

This observation is further supported by the comparison of the 2D plots for both algorithms in Figure 2.5. In these plots, the distribution for jppmuon appears less scattered, while the distribution for jppshower is more scattered. Consequently, we can infer that the directional resolution of the jppmuon algorithm is superior to that of the jppshower algorithm.

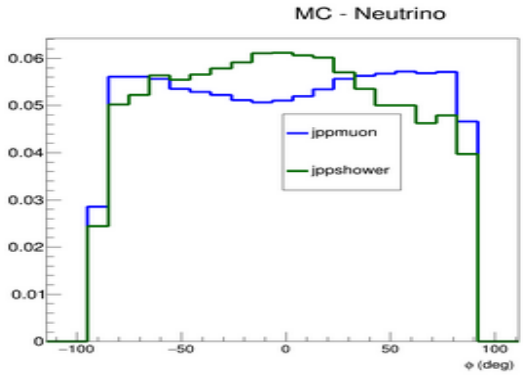

Figure 2.6: ϕ reconstruction

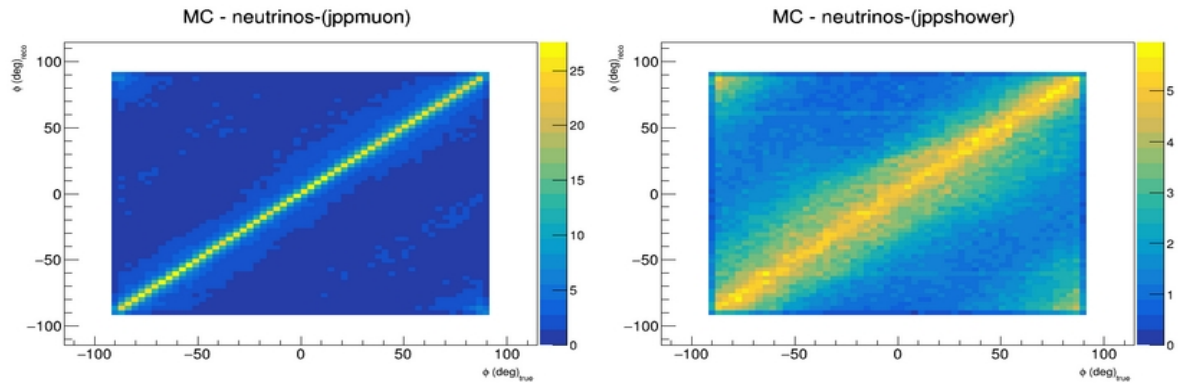

Figure 2.7: ϕ reconstruction(true vs reco)

The reconstruction of azimuth angle ϕ for both algorithms is represented in Figure 2.6 and the comparison of true vs reco is shown in Figure 2.7. Here we see the same pattern as reconstruction of $\cos\theta$ shown in Figure 2.5. The reconstruction for jppshower is more scattered than jppmuon algorithm.

Since the ϕ represents the direction (azimuthal angle), so we can conclude the same as reconstruction of $\cos\theta$ for Figure 2.7 which is the directional resolution of the jppmuon algorithm is superior to that of the jppshower algorithm.

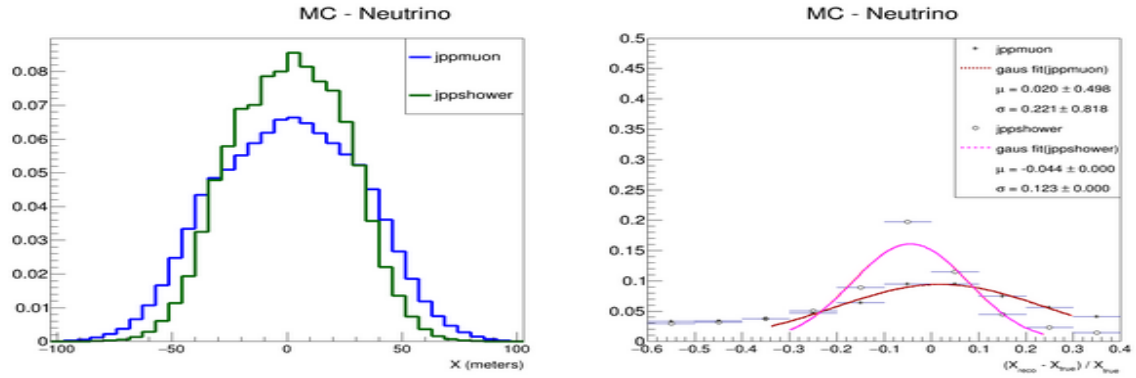

Figure 2.8: Position X (in meters) reconstruction

Figure 2.8 shows the reconstructed position X for each algorithm. The ξ plot reveals that jppmuon has a positive bias of 0.02 with a larger spread of 0.221, while jppshower has a bias of -0.04 and a spread of 0.12, indicating slight differences between the two algorithms.

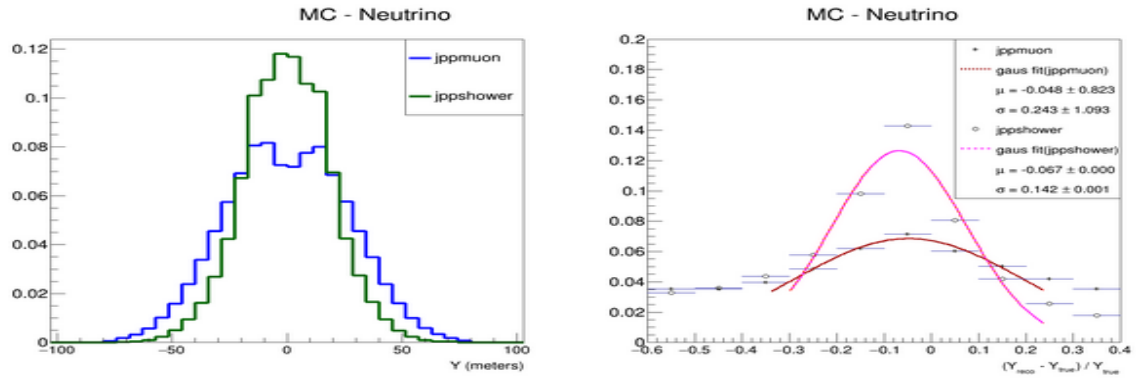

Figure 2.9: Position Y (in meters) reconstruction

Figure 2.9 presents the reconstructed position Y for both algorithms. The ξ plot shows that jppmuon and jppshower have similar negative biases of -0.05 and -0.07, respectively. However, jppmuon exhibits a wider spread of 0.243 compared to jppshower's spread of 0.142, though the overall difference between the algorithms is minimal.

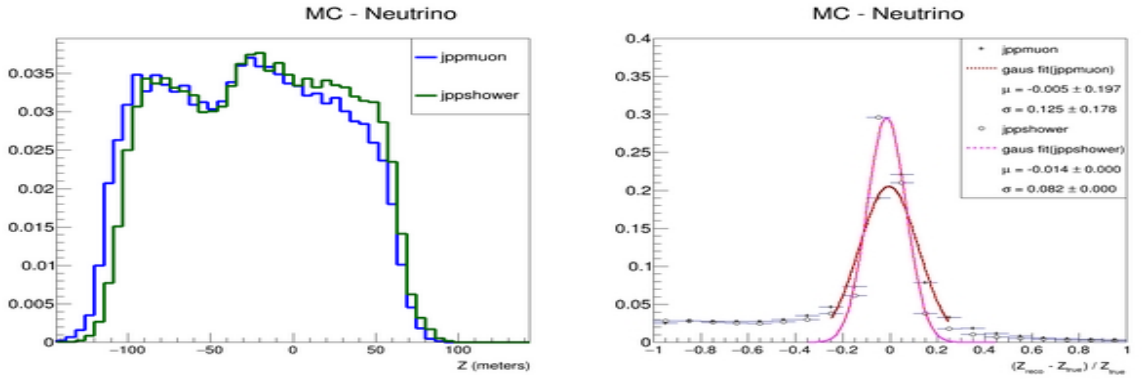

Figure 2.10: Position Z (in meters) reconstruction

Figure 2.10 illustrates the reconstructed position Z for both algorithms. The ξ plot shows minimal bias for both jppmuon and jppshower, around -0.01. However, jppmuon has a slightly larger spread of 0.125 compared to jppshower's 0.082.

By comparing the distributions ofξ variable for position, we can say that there is more spread for jppmuon algorithm than jppshower with the least bias and spread for position Z. Despite these differences in spread, the overall performance of the two algorithms remains quite similar across all reconstructed positions (X, Y, and Z).

2.4.2 For Muons

In this section, the reconstruction results from the jppmuon algorithm are obtained after cut 2 is applied, while for the jppshower algorithm, they are obtained with cut 4.

The reconstructed energy by jppmuon has maximum around 20 GeV with a extra peak on the right side but for jppshower it is centered around 100GeV.

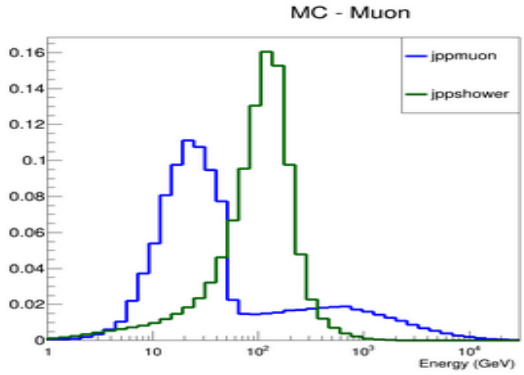

Figure 2.11: Energy reconstruction

Figure 2.12, represents 2D (reco vs true) and fit of projection of bin no 34 with mean 17.76 GeV and standard deviation 6.51 GeV. In the projection we can clearly see the second peak on right side. As mentioned before the reason for this behaviour is still being investigated. There is linearity observed from 40 GeV to until 100 GeV in 2D plot for jppmuon. After 100 GeV the saturation is observed. From 60 to 2000 GeV two peaks are overlaping but after 2000 we can see two distinct peaks. The red line represents the perfect reconstruction.

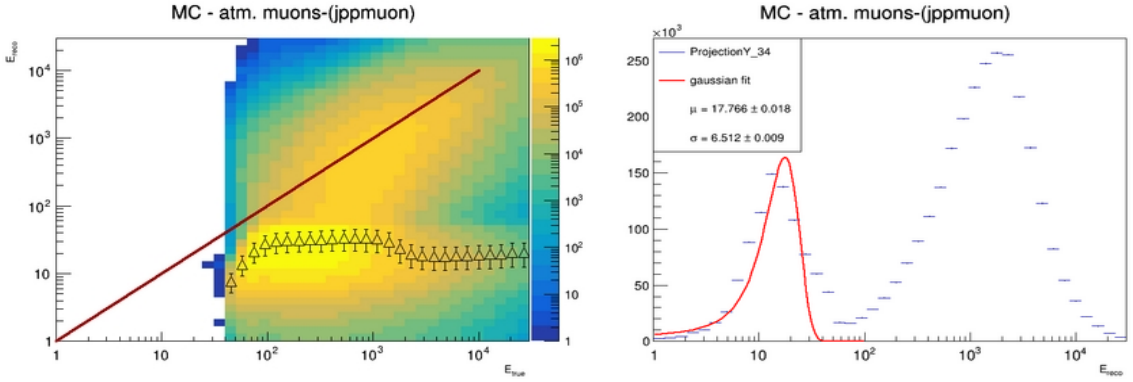

Figure 2.12: Energy 2d reconstruction and Gaussian fit for a projection of bin no 34 (Energy in GeV)

Figure 2.13 represents energy 2D plot (reco vs true) and projection of bin no 34 given by jppshower. The fit results for projection are mean 176.8 GeV and standard deviation 67.96 GeV. The reconstructed E is linear in 2D plot for all the range. But it deviates after 200 GeV from perfection reconstruction.

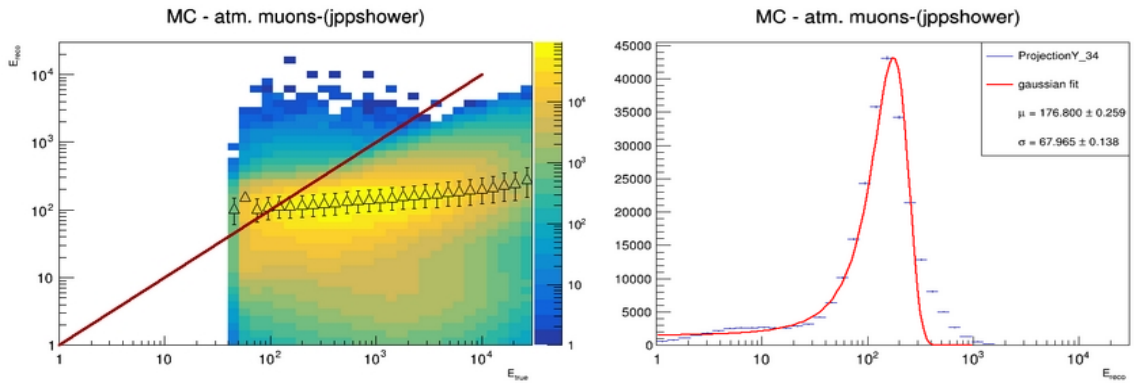

Figure 2.13: Energy 2d reconstruction and Gaussian fit for a projection of bin no 34 (Energy in GeV)

By comparison of 2D plots (reco vs true) for Energy, we can conclude that the energy is reconstructed better by jppshower algorithm than jppmuon.

We know that atmospheric (cosmic) muons can not pass through the earth so in true all muons are downgoing. So for the simulation the true value of $\cos\theta$ is chosen greater than zero. From Figure 2.14 we can see that most of the muons are reconstructed as upgoing by both algorithms. As I said earlier, There is portion of muons which are misreconstructed as downgoing but quite less compared to good reconstruction. The right plot in Figure 2.14 represents ξ distribution. For jppmuon the bias is 0.001 almost negligible, with spread 0.064 but for jppshower there is positive bias of 0.049 with more spread of 0.245.

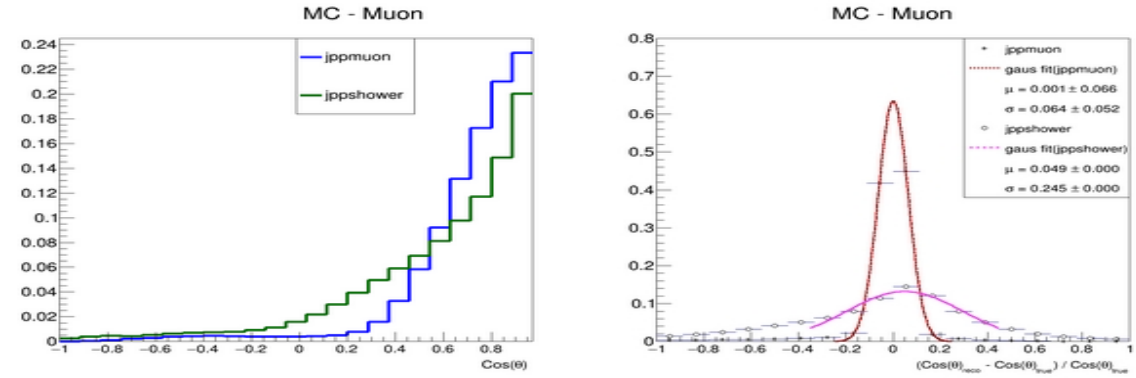

Figure 2.14: $\cos\theta$ reconstruction

Figure 2.15 shows reconstruction of ϕ variable, with almost no difference observed between the results of the two algorithms.

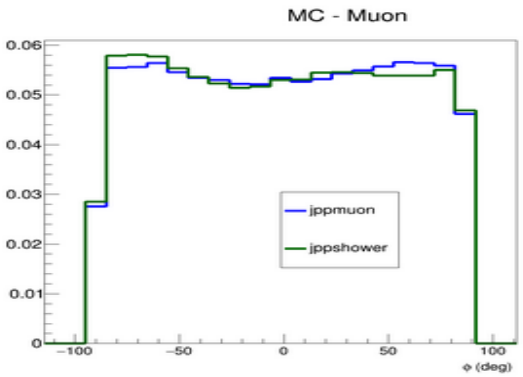

Figure 2.15: ϕ reconstruction

For the reconstruction of direction (zenith and azimuth angles), we can say that jppmuon algorithm is reconstructing better than jppshower in terms of less spread.

Figure 2.16 shows position X reconstruction for each algorithm with almost similar to each other. From the right plot of ξ, we can say that there is same bias of -0.71 for both algorithms that is quite large with slightly more spread for jppmuon (0.128) than jppshower (0.104).

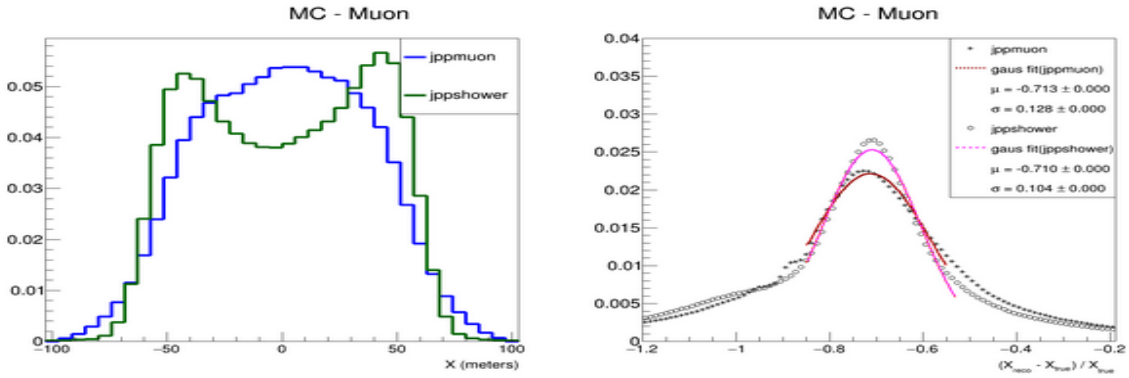

Figure 2.16: Position X reconstruction

Figure 2.17 shows almost similar reconstruction of position Y for each algorithm. The right plot of ξ shows that the bias for jppmuon is -0.76 and spread 0.133 but for jppshower bias is -0.803 and spread 0.096. The huge bias for both algorithms shows under-reconstruction.

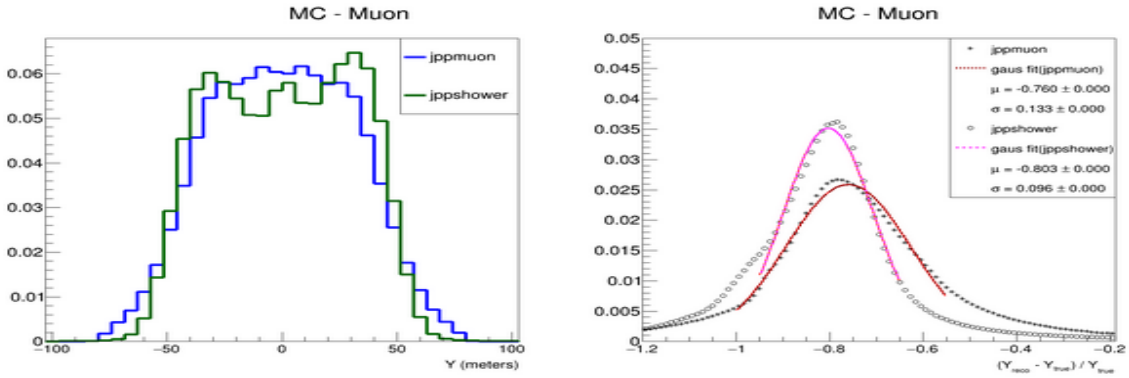

Figure 2.17: Position Y reconstruction

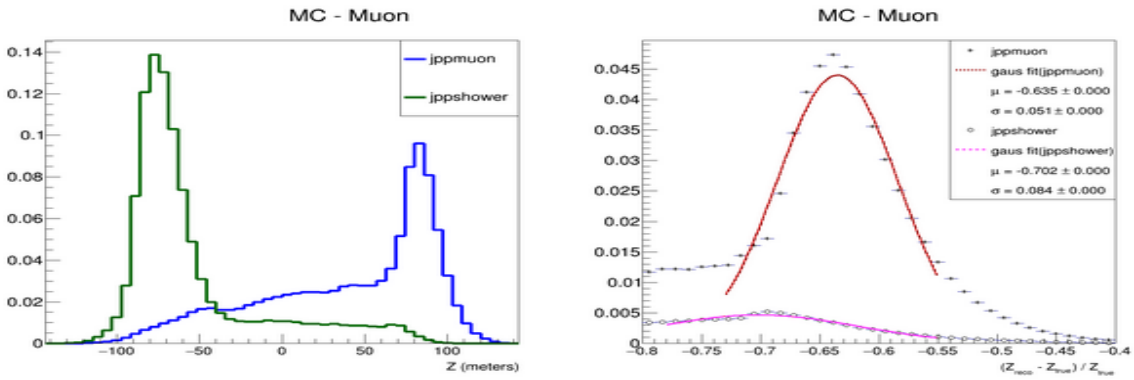

Figure 2.18: Position Z reconstruction

Figure 2.18 shows reconstruction of position Z. The left plot could be explained with the help of ξ distribution in right plot. There is less bias for jppmuon (-0.635) than jppshower (-0.702) so the events

are more under-reconstructed by jppshower. The spread for jppshower (0.084) is more than jppmuon (0.051).

As mentioned in Section 2.1, the size of can is chosen big for atmospheric muon simulation and all the events are produced on the surface of the can but these events are reconstructed inside the instrumented volume of the detector hence under-reconstruction. For the reconstruction of position of vertex, both algorithms are performing same with a huge bias and more spread for jppmuon.

2.5 Plots for Data

2.5.1 For Cut 5

The energy reconstruction for data is given in Figure 2.19. The distribution for jppmuon has maximum around 10 GeV with the extra peak on right side. For the jppshower it is centered around 80 GeV.

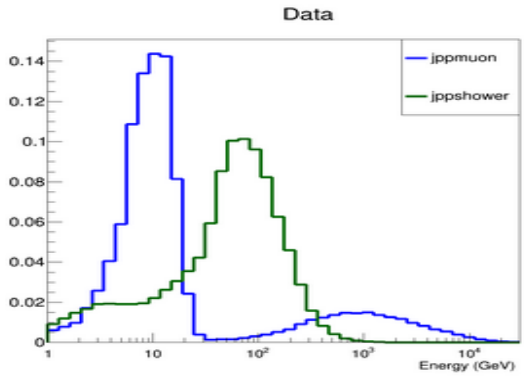

Figure 2.19: Energy reconstruction

The reconstruction of direction (zenith and azimuth angles) is shown is Figure 2.20. the reconstruction for $\cos\theta$ shows effect of cut 5. The overall reconstruction of direction for both algorithms is similar to each other.

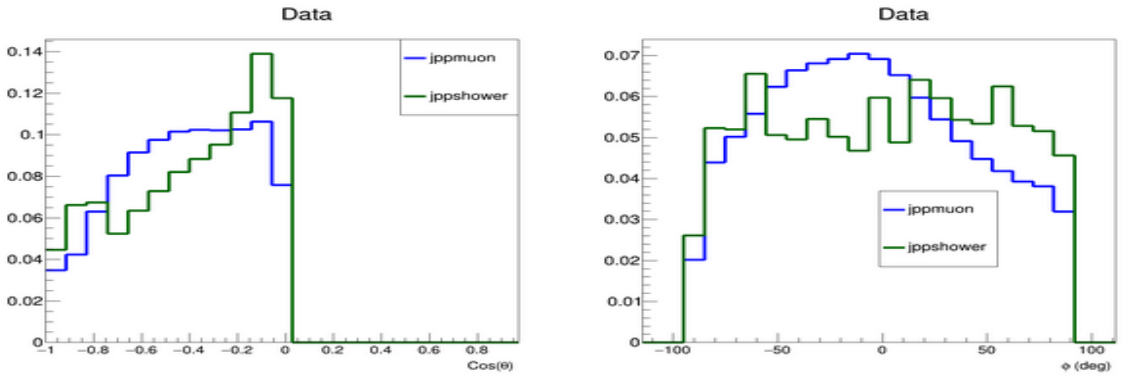

Figure 2.20: Cosine (left) and ϕ (right) reconstruction

Figure 2.21 shows the reconstruction of position of the event. The reconstruction for both algorithms is similar to each other with minor differences.

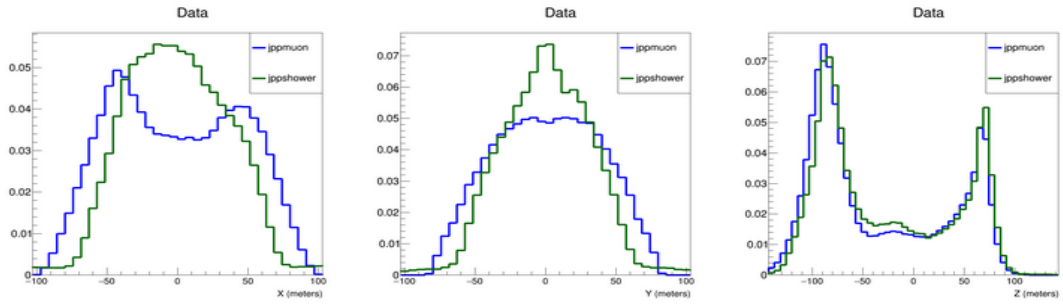

Figure 2.21: Position X(left), Y(Middle) and Z(Right) reconstruction

These all plots are reconstructed similar to atmospheric muons for cut 5 indicate that even after removing background noise and most atmospheric muons, a significant number of atmospheric muons are still mis-reconstructed. This makes it challenging to clearly observe the effect of neutrinos.

2.6 Data/MC study

In this section, experimental data and Monte Carlo (MC) comparisons are conducted for all 1,804 runs, both individually and for the entire dataset (i.e. combining all 1804 runs). The Data/MC ratio is analyzed, where the MC includes contributions from neutrinos, muons, and pure noise. This ratio is examined run by run for two key variables: energy and cosine of the zenith angle, as accurate reconstruction of these variables is essential for determining the neutrino mass hierarchy. The study focuses on three different cuts—Cut 3, Cut 4, and Cut 5. Additionally, the Data/MC ratio is analyzed for the full dataset by combining all 1,804 runs. To further understand the impact of each cut, the MC components are also analyzed separately, assessing how each cut influences the different parts of the MC simulation.

2.6.1 Analysis with cut 3

Figure 2.22 presents the data and MC comparison for energy for a specific run, number 8000, for each algorithm. The Data/MC ratio is calculated for each bin and then fitted with a constant function. The resulting ratio from the fit is 0.81 for the jppmuon algorithm and 0.84 for the jppshower algorithm.

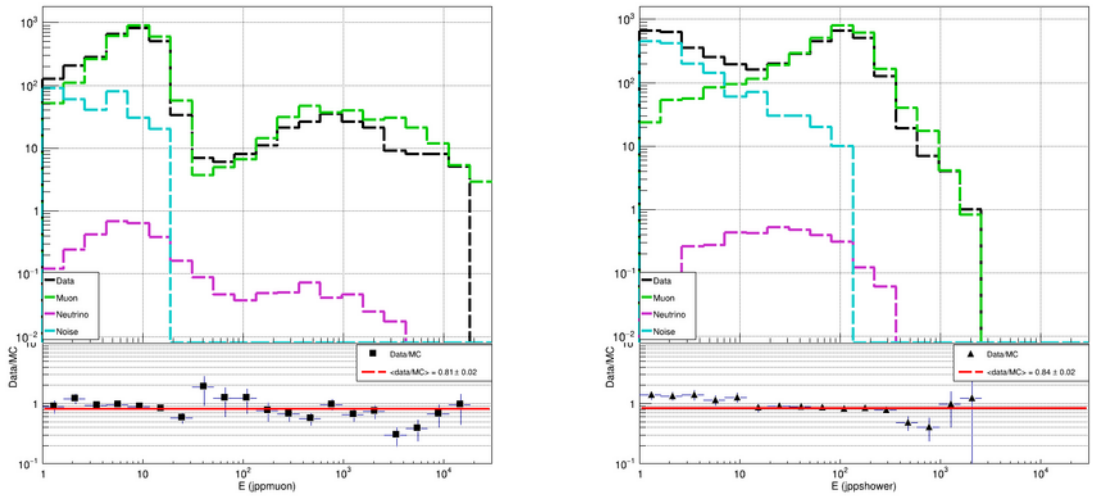

Figure 2.22: Data and MC comparison for a specific run no 8000 for jppmuon (left) and jppshower (right)

The ratio from the fit for each run is plotted in Figure 2.23, illustrating the run-wise analysis. For jppmuon, this ratio is more stable and shows fewer fluctuations compared to jppshower. However, the plot for jppshower reveals an abnormally high ratio for the run range between 9600 and 9800. Both plots have higher ratio than average around run no 7680.

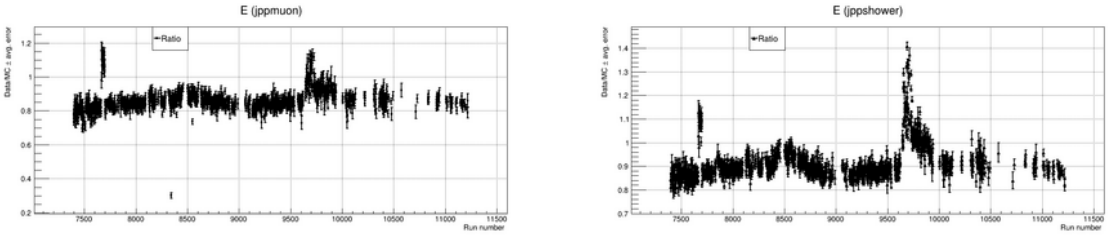

Figure 2.23: Data/MC plot for jppmuon (left) and for jppshower algorithm (right) for all runs, for E

Figure 2.24 shows the data and MC comparison for the full dataset, combining all 1,804 runs. In the comparison plot for jppmuon, the algorithm's typical behavior is evident, with a peak on the right side of the energy reconstruction for both data and muons. At lower energies (below 20 GeV), the data is predominantly influenced by background noise, while at higher energies, it is dominated by muons. These two background sources make it difficult to clearly observe the neutrino signal. The average Data/MC ratio for jppmuon is 0.88 and for jppshower 0.93 which aligns with Figure 2.23.

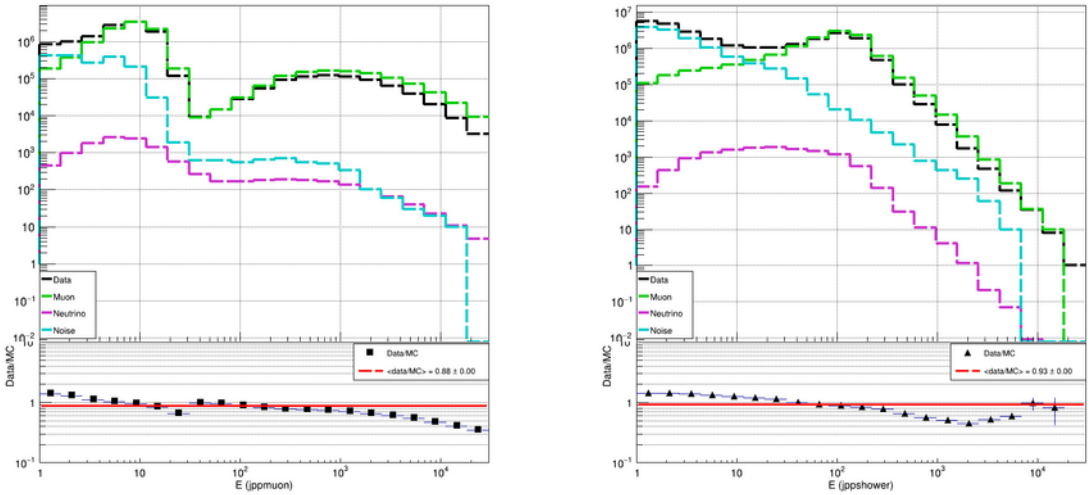

Figure 2.24: Data and MC comparison for full statistics, for jppmuon (left) and jppshower (right) for E

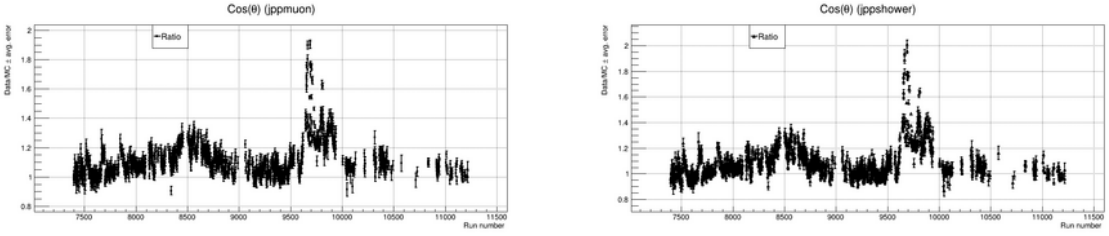

Figure 2.25: Run wise analysis of Data/MC ratio for $\cos\theta$

Figure 2.25, shows the run wise analysis of data/MC ratio. The overall fluctuation of ratio for all runs is same for both algorithms with an abnormally high ratio for the run range between 9600 and 9800.

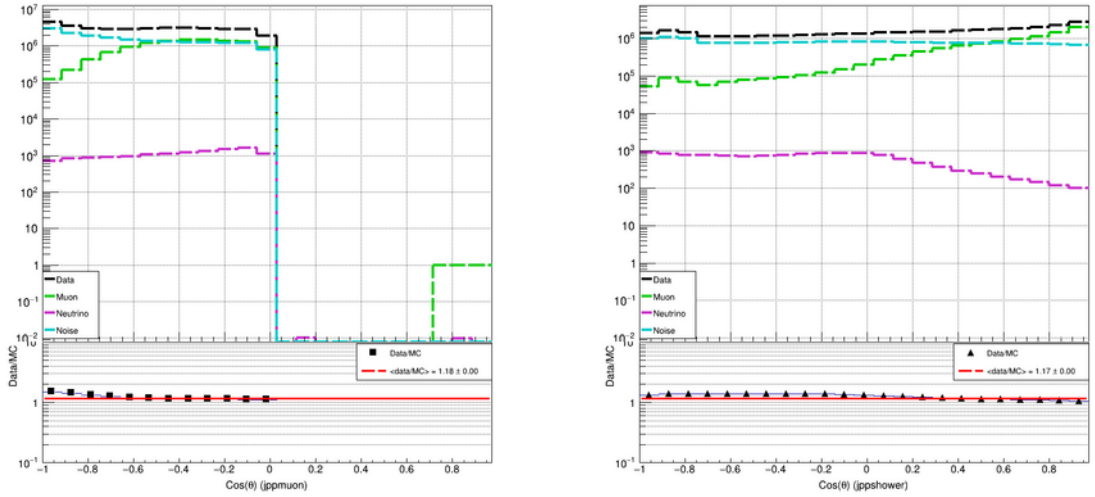

Figure 2.26: Data-MC comparison for $\cos\theta$

Figure 2.26 presents data-MC comparison for full statistics for $\cos\theta$. In the data and MC comparison plots, the background contributions from noise and muons do not follow any specific pattern. The average Data/MC ratio is 1.18 for jppmuon and 1.17 for jppshower, indicating similar overall behavior between the two algorithms.

2.6.2 Analysis with cut 4

In this section, we analyze the impact of the "number of triggered PMTs greater than 12" condition on both the simulation and experimental data. As shown in Figure 2.27, the Data/MC ratio follows a similar pattern across all runs for both algorithms. However, the previously observed abnormally high ratio in the run range between 9600 and 9800, as seen in Figure 2.23, has been reduced after applying this condition, making it a good cut for that run range. But the high ratio around run no 7680 is still there.

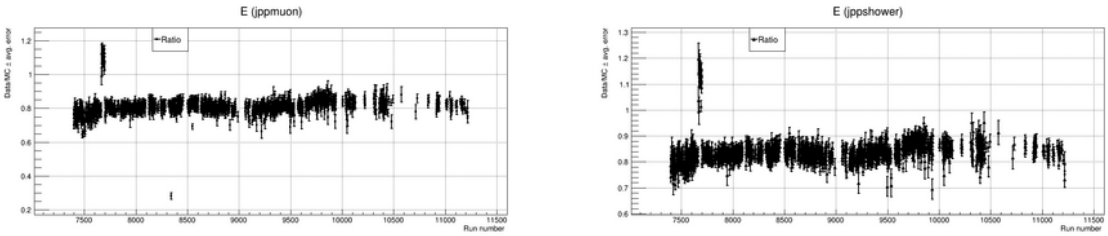

Figure 2.27: Data/MC plot for jppmuon (left) and for jppshower algorithm (right) for all runs

From Figure 2.28, the impact of the "number of triggered PMTs greater than 12" condition is clearly visible, particularly in the lower energy range, where it significantly reduces background noise. Comparing with Figure 2.24, we observe that pure noise has been reduced from 10^5 to 10^2 for jppmuon and from 10^6 to 10^3 for jppshower at lower energies. The data reduction for jppmuon ranges from 10^6 to 10^4, and for jppshower with slight variation. For muons, the reduction is similar for both algorithms, from 10^5 to 10^4. Importantly, this condition has the least impact on neutrinos. The average Data/MC ratio is 0.83 for jppmuon and 0.85 for jppshower, indicating similar overall behavior between the two algorithms.

If we compare the ratio fit in Figure 2.28 and 2.24 for each algorithm, we can say that the average ratio is reducing but it becomes more consistent. For jppshower in Figure 2.28 the ratio is more consistent

until 200 GeV but in Figure 2.24 it is deviating for lower and higher energies.

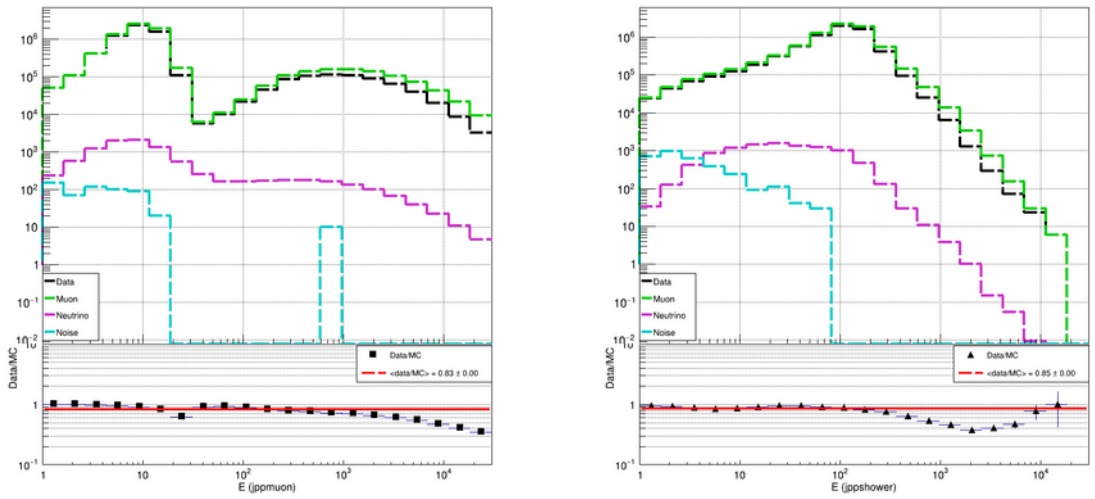

Figure 2.28: Data and MC comparison for full statistics, for jppmuon (left) and jppshower (right) for E

Figure 2.29 represents Run wise analysis and data-MC comparison for$\cos\theta$The condition does not affect a specific range but instead affects the entire range of $\cos\theta$uniformly. It has the greatest impact on pure noise, followed by data, muons, and finally neutrinos, which are affected the least. The average Data/MC ratio is 0.86 for jppmuon and 0.85 for jppshower, showing that both algorithms exhibit similar overall behavior.

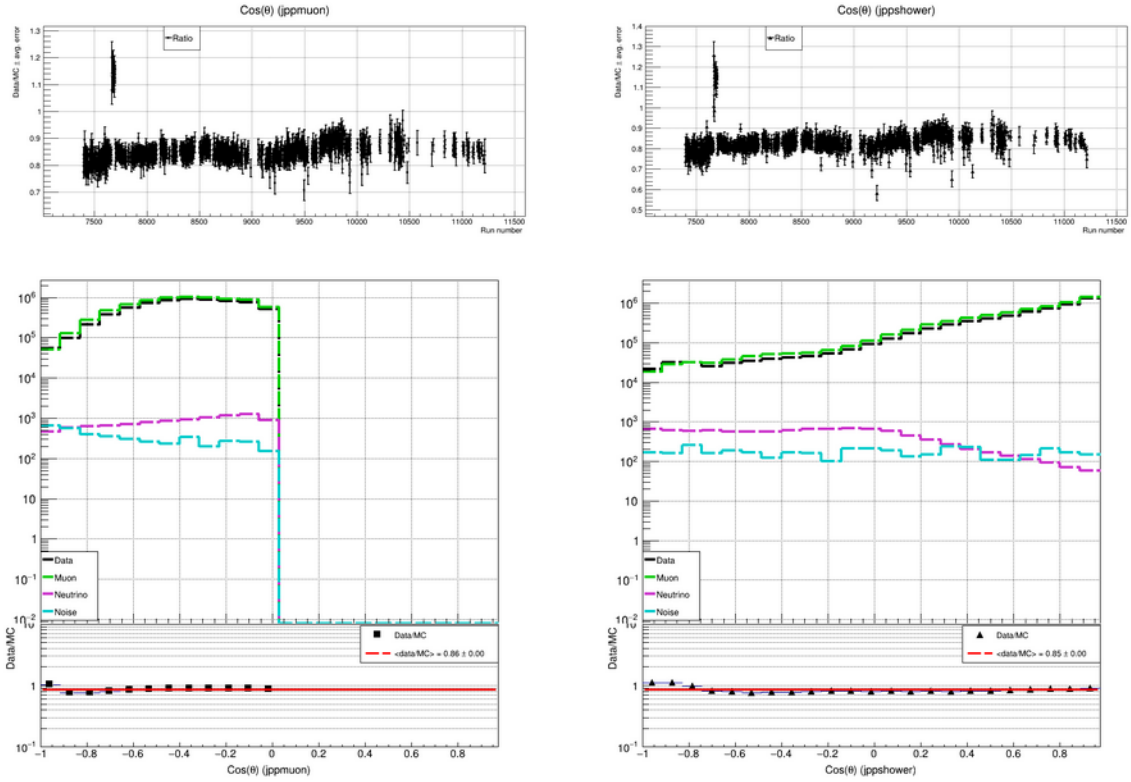

Figure 2.29: Run wise analysis of Data/MC ratio and data-MC comparison for $\cos\theta$

2.6.3 Analysis with cut 5

The cut 5 is more important from physics point of view since it requires the condition "reconstructed as upgoing by both algorithm" so removing mostly atmospheric muons and in order to study oscillation we need to study neutrinos passing through earth. Figure 2.30 shows data/MC ratio for all runs, for each algorithm. The overall pattern is same for both algorithms with higher ratio around run no 7680.

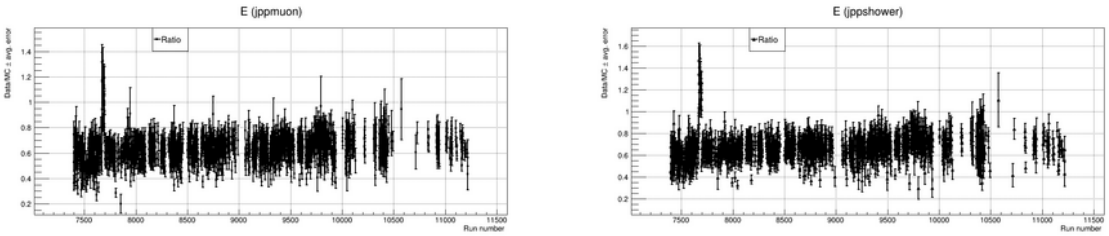

Figure 2.30: Data/MC plot for jppmuon (left) and for jppshower algorithm (right) for all runs

Figure 2.31 shows the Data and MC comparison for each algorithm for Energy. Since the selection is applied using reconstructed direction ($\cos\theta$) in cut 4, we don't see a specific range which is affected. The overall pattern is same as Figure 2.28. The average Data/MC ratio is 0.75 for jppmuon and 0.76 for jppshower, showing that both algorithms exhibit similar overall behavior. The average data/MC ratio is reduced than the last cut (Figure 2.28).

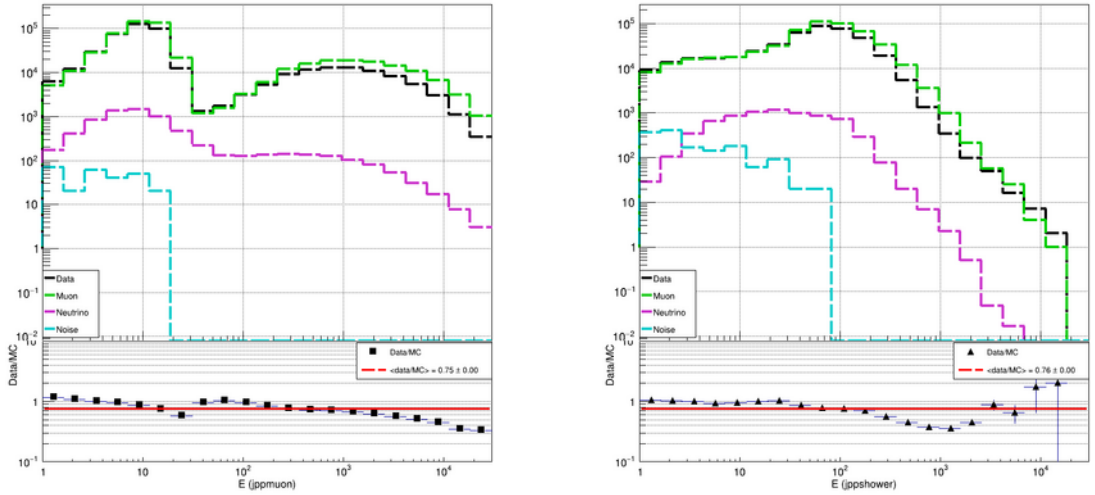

Figure 2.31: Data and MC comparison for full statistics, for jppmuon (left) and jppshower (right) for E

Figure 2.32 shows Run wise analysis of Data/MC ratio and data-MC comparison for $\cos\theta$ for each algorithm. Data-MC comparison for jppshower reflect the cut 5. As for jppmuon, there is no specific range. But after comparing with Figure 2.29, we can say that it affected the overall range by factor of 10 for jppmuon. The average Data/MC ratio is 0.83 for the jppmuon algorithm and 0.82 for the jppshower algorithm.

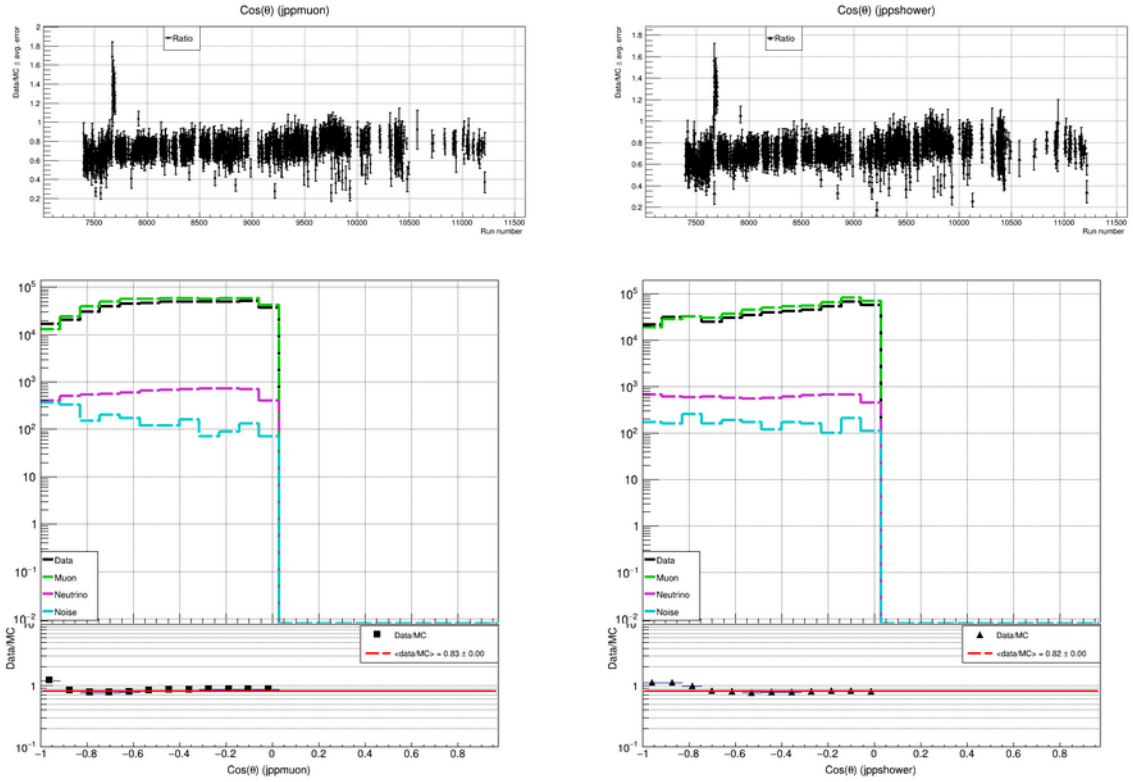

Figure 2.32: Run wise analysis of Data/MC ratio and data-MC comparison for $\cos\theta$

Chapter 3

Conclusions and Discussions

Determining the neutrino mass hierarchy requires accurate reconstruction of $\cos\theta$ and energy. For detectors like ORCA, which lack protective shielding, the most challenging aspect is effectively removing background signals, particularly from atmospheric muons and bioluminescence. Overcoming these background challenges is crucial for isolating the neutrino signals needed for mass hierarchy determination. The goal of this report could be divided into 3 parts :

First, verifying the reconstruction of each variable given by each algorithm across various cuts (cut 1, 2, 3, 4). The analysis focuses on studying the reconstructed variables by both algorithms using reco vs true plots, along with corresponding 1D distributions. The efficiencies between cut 1 and cut 2 for jppmuon, as well as between cut 2 and cut 4 for jppshower, are calculated to estimate the number of events removed. From Table 2.2, it is evident that the condition "number of triggered PMTs greater than 12" effectively reduces background noise.

Second, comparing performances for both algorithms for neutrino and muon simulations. We know muons are track like events so we expect jppmuon algorithm to reconstruction better which is not the case for muons. We see the typical behaviour for energy reconstructed by jppmuon having two peaks. The reason for extra peak is still being investigated. From reconstructed energy, we can say that jppshower reconstructs energy better with huge range where linearity is followed. As for the direction (zenith and azimuth) we can conclude that jppmuon reconstructs better than jppshower with less spread. For the position of vertex for neutrinos, there is overall little negative bias with more spread for jppmuon but for muons the position is under-reconstructed explaining all the true events produced on the surface of can being reconstructed inside instructed volume. The plots for data for cut 5 shows the dominated part of muons in data.

And last Data/MC ratio is studied to check quality of simulation for a sample of runs and full statistics. The Data/MC ratio is studied for 3 cuts : cut 3, 4, 5 for two variables Energy and $\cos\theta$ It is observed that with each additional cut, the average ratio gradually decreases. Additionally, for some runs, the ratio is above average for cut 3, but this is reduced with the application of cut 4. Data and MC comparisons are performed for the full dataset to assess how each component is impacted by the cut. Analysis with cut 4 reveals that the condition "number of triggered PMTs greater than 12" primarily affects the lower energy range. Incorporating these Data/MC studies could help improve future simulations.

Bibliography

[1] The KM3NeT Collaboration, “Determining the Neutrino Mass Ordering and Oscillation Parameters with KM3NeT/ORCA”. *Eur. Phys. J. C* 82, 26 (2022).

[2] Hofestädt, Jannik, "Measuring the neutrino mass hierarchy with the future KM3NeT/ORCA detector" Feb, 2017

[3] S. H. D. Haddock, M. A. Moline and J. F. Case, "Bioluminescence in the Sea" *Annu. Rev.* Mar. Sci. 2, 443 (2010).

[4] Illénia Salvadori. “Study of atmospheric neutrino oscillations with the ANTARES neutrino telescope”, PhD thesis. Aix Marseille Université, 2018.

[5] S. Adrián-Martínez et al. “Letter of intent for KM3NeT 2.0”. In: *Journal of Physics G: Nuclear and Particle Physics* (2016).

[6] Tommy Ohlsson and Håkan Snellman. “Three flavor neutrino oscillations in matter”. In: *Journal of Mathematical Physics* (2000).

[7] Dziewonski, Adam M.; Anderson, Don L. (June 1981). "Preliminary reference Earth model", *Physics of the Earth and Planetary Interiors.* 25 (4): 297–356

[8] Simon Bourret et al. Phd Thesis "Neutrino oscillations and Earth tomography with KM3NeT-ORCA". (2017)

Appendix A

Appendix A

A.1 Analysis for Neutrinos

A.1.1 For Cut 1 and 3

In this section, the reconstruction provided by the jppmuon algorithm is obtained after applying cut 1, while for the jppshower algorithm, it is obtained after applying cut 3.

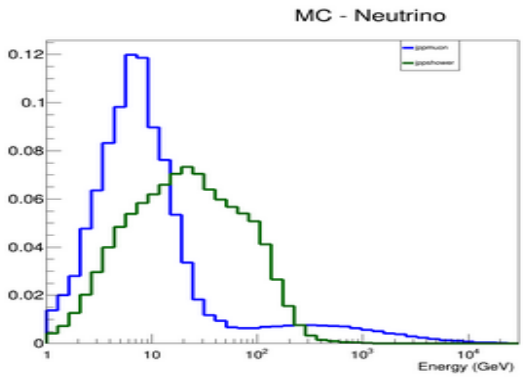

Figure A.1: Energy reconstruction

Figure A.1 represents the Energy reconstructed by each algorithm. For jppmuon, we can see the typical behaviour of algorithm.

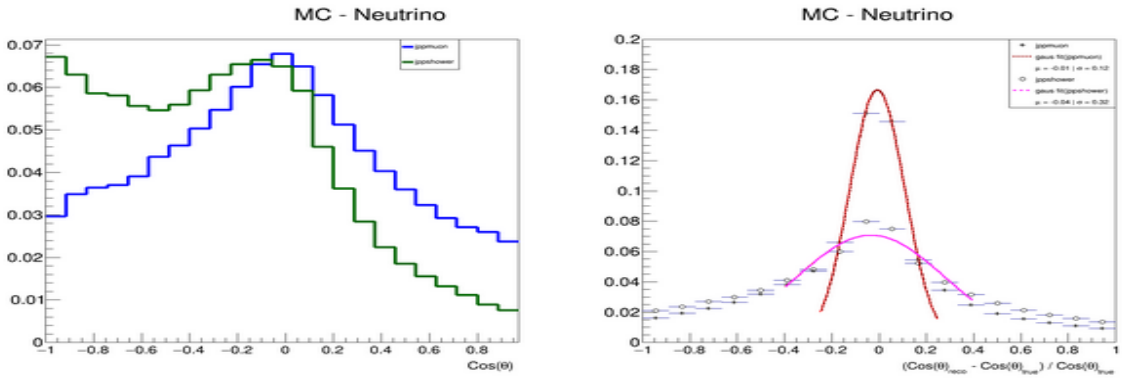

Figure A.2: Cosine reconstruction

The reconstruction of cosine of zenith angle is given in the left side of Figure A.2. For the jppmuon algorithm, the distribution is centered around zero which represents that the most of the events are re-

constructed horizontally. For jppshower algorithm, we can see that there are less events reconstructed downgoing($\cos\theta$)>0), since the jppshower algorithm is applied only for those events which are reconstructed upgoing($\cos\theta$)<0) by jppmuon algorithm. So the events which are reconstructed upgoing by jppmuon algorithm are more likely to be true upgoing and reconstructed more in the upgoing direction by the jppshower algorithm.

The plot to the right side of the Figure A.2 represents the variable ξ for cosine. There is very less bias for the both algorithms but the spread of ξ for jppmuon is less than the jppshower.

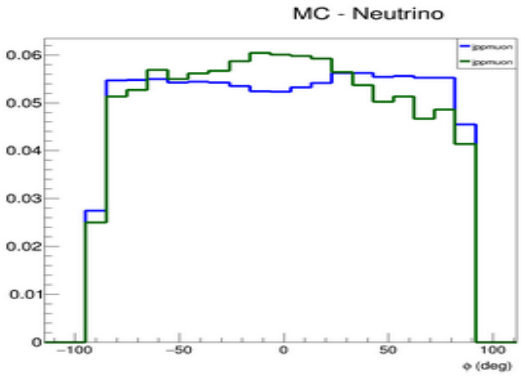

Figure A.3: ϕ reconstruction

The reconstruction of ϕ is shown in the Figure A.3 with similar pattern for both algorithms.

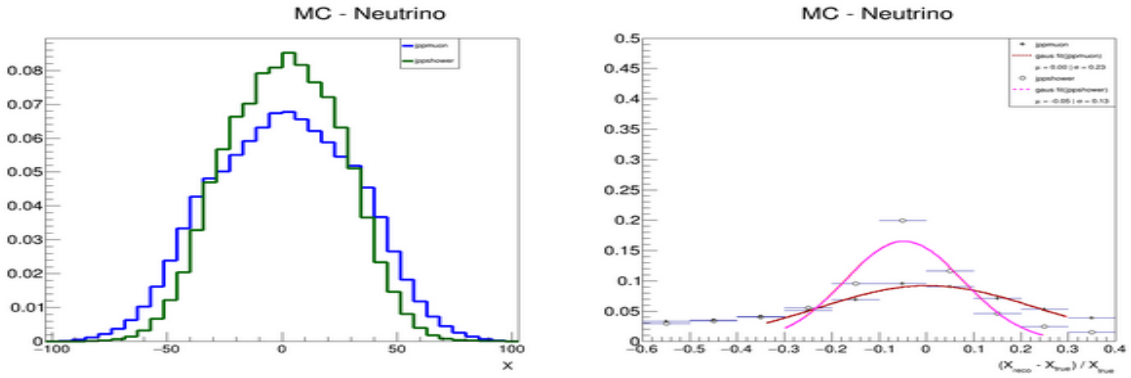

Figure A.4: Position X reconstruction

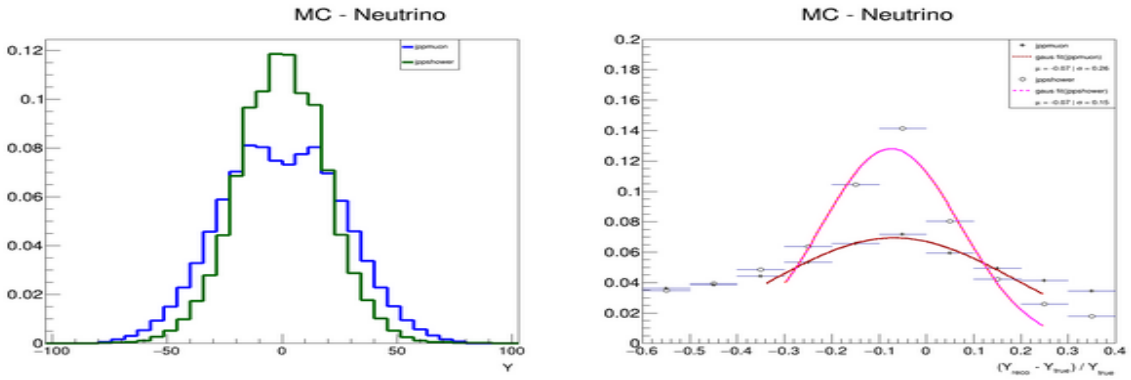

Figure A.5: Position Y reconstruction

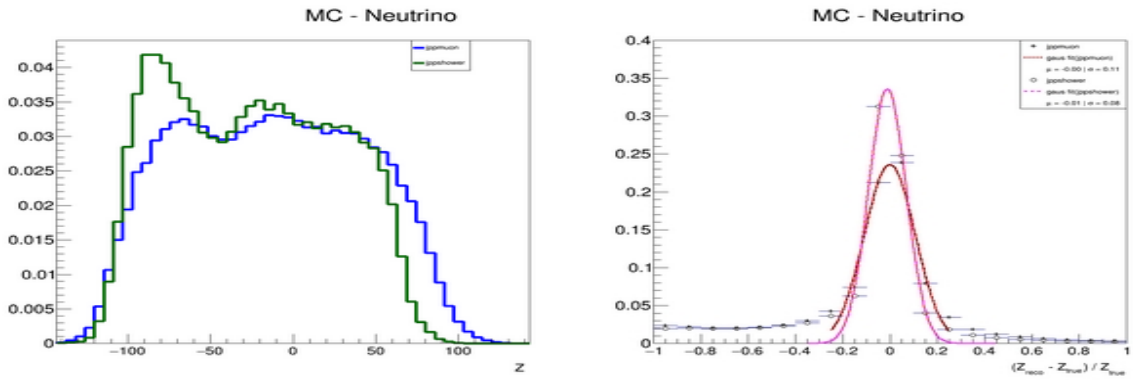

Figure A.6: Position Z reconstruction

The reconstruction of position where neutrino is interacting inside the detector, is shown in the plots from Figure A.4 to Figure A.6. By comparing the ξ plots for position on the right side, we can conclude that there is very little bias with the least spread for position Z.

A.1.2 For Cut 2 and 4

In this section, the reconstruction results from the jppmuon algorithm are obtained after cut 2 is applied, while for the jppshower algorithm, they are obtained with cut 4.

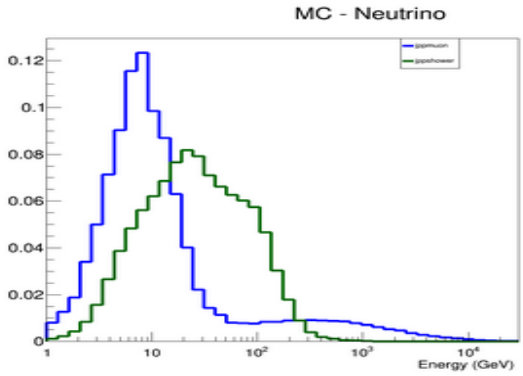

Figure A.7: Energy reconstruction

If we compare Figure A.7 with the Energy reconstruction in Figure A.1, we can see that lower energetic events are removed for this analysis. This tells that the condition "no of triggered PMTs more than 12" affects the lower energetic events which could be beneficial in removing background noise events which are lower energetic.

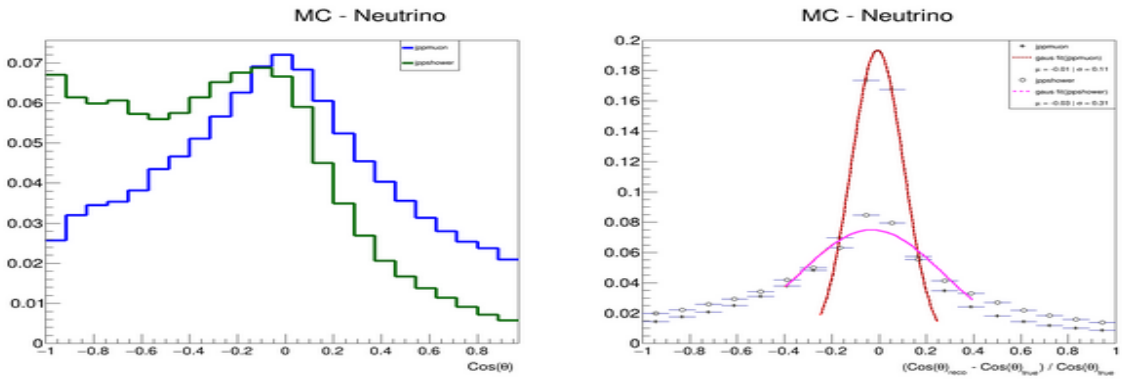

Figure A.8: Cosine reconstruction

By comparing Figure A.8 and A.2, we can conclude that the extra condition is affecting all the range equally for reconstructed cosine for both algorithms and for ξ as well, so the overall pattern does not change.

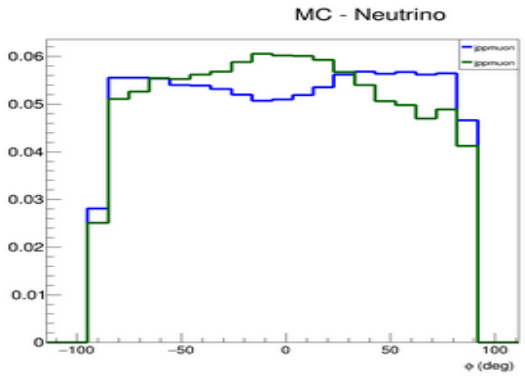

Figure A.9: ϕ reconstruction

The overall behaviour does not change much for reconstructed ϕ from the Figure A.3.

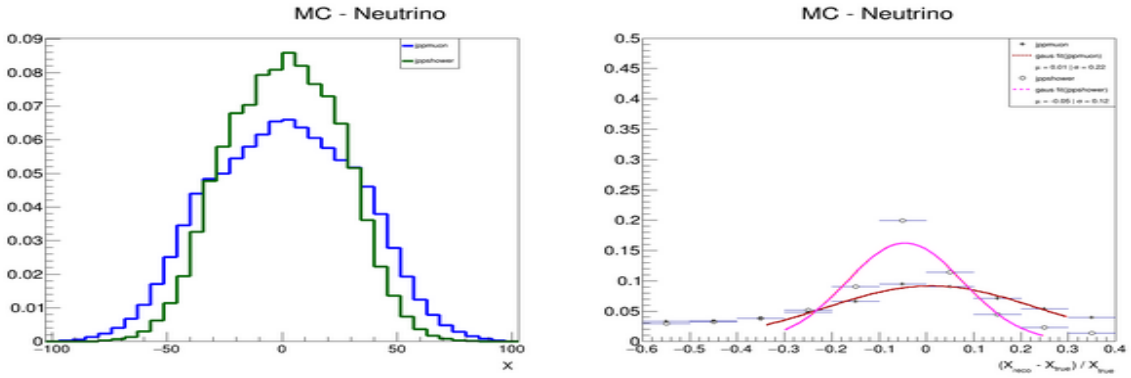

Figure A.10: Position X reconstruction

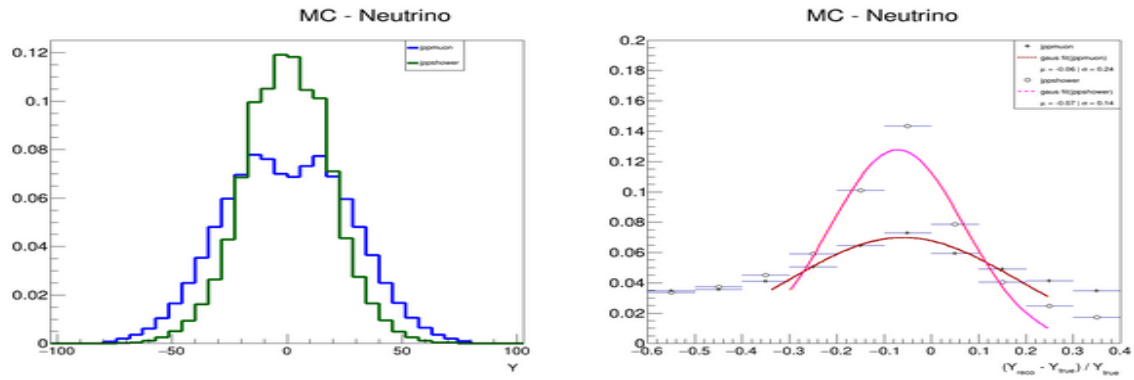

Figure A.11: Position Y reconstruction

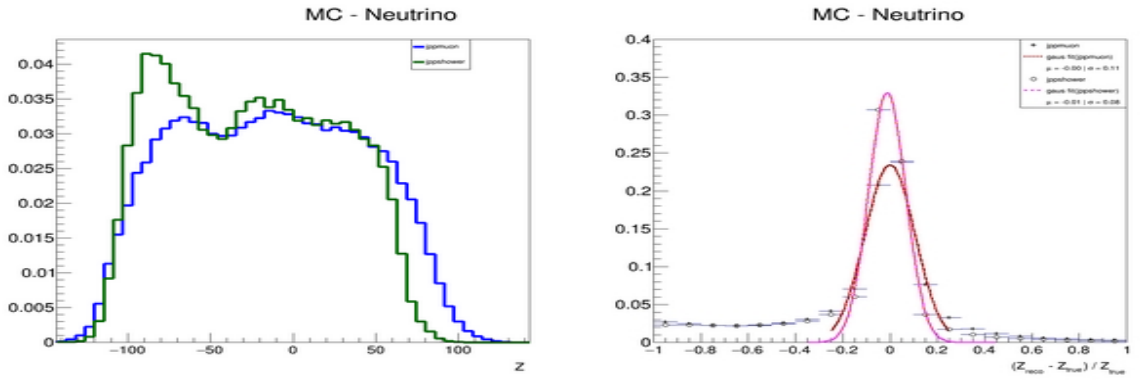

Figure A.12: Position Z reconstruction

The reconstructed position could be commented the same since the overall pattern has not changed from reconstructed position in Section A.1.1 with the same good reconstruction for position Z.